Modeling and Stability Analysis of Single-Phase Microgrids Controlled in Stationary Frame

Nima Amouzegar Ashtiani, *Graduate Student Member, IEEE*, S. Ali Khajehoddin, *Senior Member, IEEE*, and Masoud Karimi-Ghartemani, *Senior Member, IEEE*

***Abstract*—Modern microgrids are transitioning toward having an increasing portion of grid-forming (GFM) converters to support nontraditional sources, such as renewable energy and energy storage systems, while aiming to improve system stability, reliability, power rating, and flexibility. Understanding the interaction among parallel GFM converters to guarantee the microgrid stability within various operating conditions is necessary. For single-phase systems, when the controllers are implemented in the rotating frame to facilitate the stability analysis and design, the required orthogonal signal generation (OSG) units degrade the system stability. On the other hand, when the controllers are implemented in the stationary frame to avoid OSG-related problems, the stability analysis becomes particularly challenging due to nonlinearities and mixed dc and ac state variables. In this article, an approach is proposed to systematically model and perform stability analysis for a single-phase microgrid with stationary frame controllers. The approach is based on defining a complementary system that allows transformation to the synchronous rotating frame without introducing time-varying (double-frequency) terms and without altering the stability properties. The accuracy of the proposed modeling approach is verified using simulations and experimental results.**

***Index Terms*—Microgrid stability, parallel inverters, single-phase microgrid, stationary frame control.**

I. Introduction

SINGLE-PHASE grid-forming (GFM) converters are increasingly used in single-phase microgrids, such as shown in Fig. 1, mostly for remote areas where there is no access to the main grid or for sensitive applications, such as hospitals [1]–[3]. As their level of penetration increases, the GFM converters play a more significant role in controlling the voltage, frequency, and system stability. This distinguishes them from grid-following (GFL) converters, which do not directly and dynamically participate in the grid-voltage support.

A single-phase control system can be implemented in the stationary frame or the synchronous rotating frame. In both frames, output-feedback, such as the proportional–resonant in the stationary frame or the proportional–integral in the rotating frame, state-feedback, or more complicated compensators can be used. However, an orthogonal signal generation (OSG) unit to enable Park's ($\alpha\beta \rightarrow dq$) transformation [4] is required in rotating frame. Orthogonal signals are generated by phase-shift methods, such as time-domain delay [5], the Hilbert transform [6], or second-order generalized integrator (SOGI) [7]. While the steady-state performance of the phase-shift approaches is acceptable, these OSG methods add undesirable dynamics leading to slower and oscillatory responses. Fictive axis emulation (FAE) method [8] generates orthogonal signals by emulating β-axis circuit in the processor. However, its accuracy depends on system parameters, and a parameter mismatch may lead to steady-state errors in the orthogonal signals, which makes the system responses more oscillatory. In reference-based OSG method [9], the orthogonal signal is generated based on the reference values in the rotating frame. This method is useful only when the reference values are available in the rotating frame. As the literature indicates and this article also confirms, the stability analysis and design of the control system in the rotating frame are simple, but the OSG units compromise the performance and limit the stability margins. Contrarily, the implementation of the control system in the stationary frame provides more robust performances with improved stability margins, but the stability analysis and design become challenging due to mixed ac/dc variables and nonlinear dynamics [10]. Fig. 2 briefly compares advantages and disadvantages of the control systems implemented in the stationary frame and rotating frame.

In [11], the stability analysis is addressed for two uninterruptible power supply systems. However, the nonlinearity caused

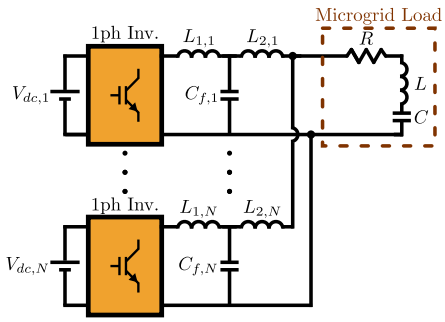

Fig. 1. Single-phase microgrid with parallel inverters.

Manuscript received April 27, 2021; revised October 5, 2021 and December 21, 2021; accepted January 22, 2022. Date of publication January 31, 2022; date of current version March 24, 2022. Recommended for publication by Associate Editor A. Yazdani. *(Corresponding author: Nima Amouzegar Ashtiani.)*

Nima Amouzegar Ashtiani and S. Ali Khajehoddin are with the Department of Electrical and Computer Engineering, University of Alberta, Edmonton, AB T6G 1H9, Canada (e-mail: amouzegar@ualberta.ca; khajeddin@ieee.org).

Masoud Karimi-Ghartemani is with the Department of Electrical and Computer Engineering, Mississippi State University, Starkville, MS 39762 USA (e-mail: karimi@ece.msstate.edu).

Color versions of one or more figures in this article are available at https://doi.org/10.1109/TPEL.2022.3147157.

Digital Object Identifier 10.1109/TPEL.2022.3147157

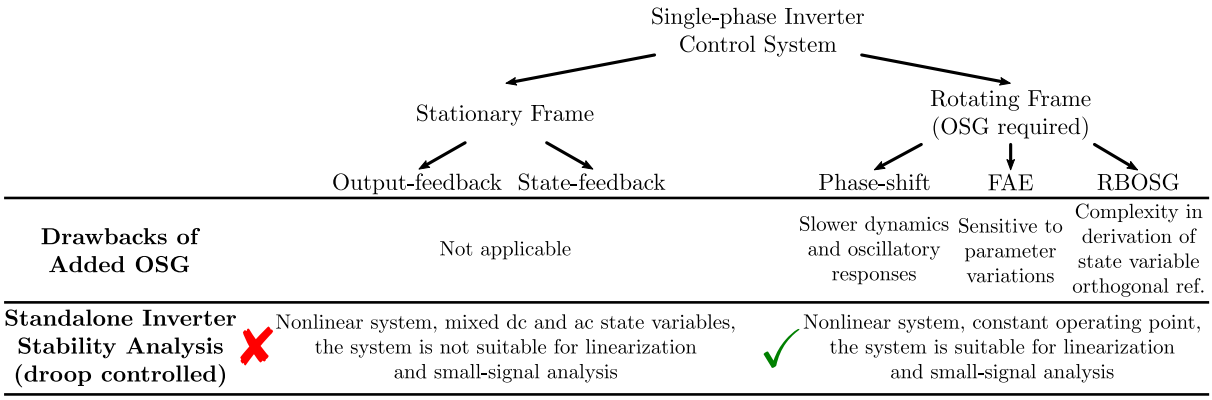

Fig. 2. Comparison of single-phase control systems in the stationary frame and rotating frame.

by the droop terms is not considered. In [12], load sharing strategies are proposed for droop-controlled inverters in microgrids. However, the interaction among inverters is not discussed. A small-signal stability analysis is carried out by using the common rotating frame analysis for three-phase systems in [13] and [14]. However, this analysis and similar three-phase analysis approaches are not applicable to single-phase systems controlled in the stationary frame due to the lack of orthogonal ac variables to transform the system to the rotating frame. In [15], the Nyquist stability criterion is used. However, it cannot predict how a parameter variation may change the system pole locations.

In summary, in the rotating frame, because the dynamics originated from OSGs is not modeled, the accuracy of the entire model and the stability analysis are questionable. On the other hand, in the stationary frame, the stability analysis is a challenge due to mixed ac/dc variables with nonlinear dynamics. Conventionally, the control implementation and modeling are both done either in the stationary or in the rotating frame. Also, both methods have drawbacks, discussed earlier, that affect the stability and design of the system. This article uses the preferred way of implementation of the controller that is in the stationary frame without OSGs, while modeling it in the preferred frame that is the rotating frame to achieve dc quantities. This is achieved by proposing an approach based on defining a complementary imaginary system to derive the proposed large-signal (nonlinear) model of a single-phase system controlled in the stationary frame. As the large-signal model contains only dc variables, it is linearized at an operating point to find the proposed small-signal (linearized) model that can be used for stability analysis, tuning the system parameters, and studying the system sensitivity against parameter variations. Moreover, the proposed large-signal (nonlinear) model is able to represent behaviors of the fast dynamic variables of the internal loops, such as currents and voltages. Also, the proposed imaginary system does not affect the actual system dynamics because the imaginary dynamics does not interact with the system variables directly. In fact, there is no feedback from the imaginary system to the original system, and the imaginary system is only augmented with the system to allow the transformation to the rotating frame. Eventually, the proposed approach is used for modeling and stability analysis of the system containing parallel GFM inverters controlled in the stationary frame, such as shown in Fig. 1. It is worth mentioning that, to address variable frequency tracking in this article, a standalone microgrid is studied where the frequency is not fixed, and adaptive resonant controllers are successfully implemented in simulations and practice.

The rest of this article is organized as follows. Section II describes existing approaches for modeling single-phase systems. Section III presents the proposed modeling approach. The state-space equations of the microgrid in the stationary frame are derived in Section IV. Section V presents the state-space equations of the microgrid in the rotating frame derived by using the proposed approach. The stability analysis of the microgrid is addressed, and the proposed approach is verified by simulation and experimental results in Sections VI and VIII, respectively. Finally, Section IX concludes this article.

II. Existing Modeling Approaches

Fig. 3 illustrates two different approaches in the implementation and mathematical modeling of a single-phase droop-controlled standalone inverter. Fig. 3(a) shows the approach in the rotating frame. From the control system perspective, it requires the implementation of OSGs to generate the quadrature signals for the system conversion to the rotating frame. From the modeling point of view, OSG dynamics are not (and probably cannot be) modeled because OSG dynamics arises from its state; to convert the OSG state to the rotating frame, another OSG is needed to generate the required quadrature state for the Park's transformation. This makes the system modeling inaccurate for the control system design. Also, the system stability study based on analyzing the eigenvalues of the mathematical model, shown in Fig. 3(a), would not be fully reliable, especially, when the system operates close to its stability margins.

The alternative approach is to implement the control system and model it in the stationary frame, as shown in Fig. 3(b). In this approach, no OSGs are used in the control system. However, as shown in this figure, the system contains mixed dc and ac state variables. Moreover, due to the power calculation block and droop characteristics, the system is nonlinear. For the small-signal stability analysis, the system should be linearized around an operating point. However, due to the sinusoidal nature of

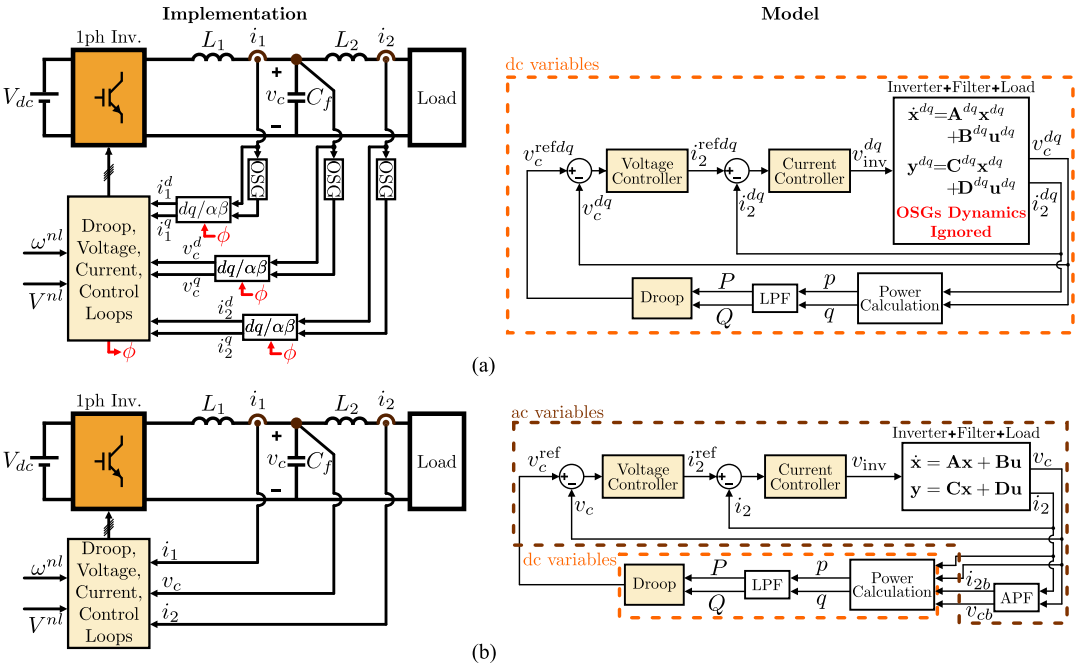

Fig. 3. Control system implementation and existing modeling approaches for a single-phase droop-controlled inverter. (a) Controlled and modeled in the rotating frame. (b) Controlled and modeled in the stationary frame.

the ac state variables, no operating point can be found for the system. Therefore, the mathematical model, shown in Fig. 3(b), is not directly usable for the stability analysis using common eigenvalue analysis.

III. Proposed Modeling Approach

As discussed in Section II, in the conventional approaches, both controller implementation and modeling are done in the same frame. However, each approach has some drawbacks that make the mathematical modeling either unusable or not fully accurate for the stability analysis. The proposed approach to resolve the aforementioned problems is shown in Fig. 4. As shown in Fig. 4(a), the control system is designed and implemented in the stationary frame similar to Fig. 3(b). Since the mathematical model in the stationary frame consists of dc and ac state variables, the stationary frame model is not proper for small-signal stability analysis. Therefore, the mathematical model should be derived in the rotating frame to contain only dc variables. For this purpose, an imaginary system is defined such that it is the same as the ac subsystem of the original system, and its input $v_c^{\text{ref}\beta}$ comes from the droop, as shown in Fig. 4(b). In this case, because the inputs of the ac subsystem of the original system $v_c^{\text{ref}\alpha}$ and the imaginary system $v_c^{\text{ref}\beta}$ are orthogonal, the imaginary system generates orthogonal variables of the ac subsystem of the original system. Therefore, the augmented system, which is the combination of the original and imaginary systems, is ready for the conversion to the rotating frame. Fig. 4(c) illustrates the transformed system that is the accurate large-signal (nonlinear) model of the single-phase droop-controlled standalone inverter in the rotating frame. This model is also suitable for the linearization and small-signal stability analysis.

In general, consider state-space equations of the original ac subsystem, containing α-axis components, are represented by

$$\dot{\mathbf{x}}^{\alpha} = \mathbf{A}\mathbf{x}^{\alpha} + \mathbf{B}\mathbf{u}^{\alpha},\ \mathbf{y}^{\alpha} = \mathbf{C}\mathbf{x}^{\alpha} + \mathbf{D}\mathbf{u}^{\alpha}. \tag{1}$$

Therefore, for the imaginary system, which contains β-axis components, the state-space equations would be

$$\dot{\mathbf{x}}^{\beta} = \mathbf{A}\mathbf{x}^{\beta} + \mathbf{B}\mathbf{u}^{\beta},\ \mathbf{y}^{\beta} = \mathbf{C}\mathbf{x}^{\beta} + \mathbf{D}\mathbf{u}^{\beta}. \tag{2}$$

After defining the imaginary system, the original and imaginary systems are combined to form the augmented system in the stationary frame. Thus, the state-space equations of the ac subsystem of the augmented system are

$$\dot{\mathbf{x}}^{\alpha\beta} = \mathbf{A}^{\alpha\beta}\mathbf{x}^{\alpha\beta} + \mathbf{B}^{\alpha\beta}\mathbf{u}^{\alpha\beta},\ \mathbf{y}^{\alpha\beta} = \mathbf{C}^{\alpha\beta}\mathbf{x}^{\alpha\beta} + \mathbf{D}^{\alpha\beta}\mathbf{u}^{\alpha\beta}$$

$$\mathbf{A}^{\alpha\beta} = \begin{bmatrix} \mathbf{A} & \mathbf{0}_{l_1\times l_1} \\ \mathbf{0}_{l_1\times l_1} & \mathbf{A} \end{bmatrix}, \mathbf{B}^{\alpha\beta} = \begin{bmatrix} \mathbf{B} & \mathbf{0}_{l_1\times l_2} \\ \mathbf{0}_{l_1\times l_2} & \mathbf{B} \end{bmatrix}$$

$$\mathbf{C}^{\alpha\beta} = \begin{bmatrix} \mathbf{C} & \mathbf{0}_{l_3\times l_1} \\ \mathbf{0}_{l_3\times l_1} & \mathbf{C} \end{bmatrix}, \mathbf{D}^{\alpha\beta} = \begin{bmatrix} \mathbf{D} & \mathbf{0}_{l_3\times l_2} \\ \mathbf{0}_{l_3\times l_2} & \mathbf{D} \end{bmatrix} \tag{3}$$

where $\mathbf{x}^{\alpha\beta}=[\mathbf{x}^{\alpha}\ \mathbf{x}^{\beta}]^T$, $\mathbf{y}^{\alpha\beta}=[\mathbf{y}^{\alpha}\ \mathbf{y}^{\beta}]^T$, and $\mathbf{u}^{\alpha\beta}=[\mathbf{u}^{\alpha}\ \mathbf{u}^{\beta}]^T$. Also, l_1, l_2, and l_3 denote the dimensions of the state vectors $\mathbf{x}^{\alpha}$, $\mathbf{x}^{\beta}$, input vectors $\mathbf{u}^{\alpha}$, $\mathbf{u}^{\beta}$, and output vectors $\mathbf{y}^{\alpha}$, $\mathbf{y}^{\beta}$ of the ac subsystem of the original and imaginary systems, respectively.

Now, similar to a three-phase system transformation to the rotating frame that is widely discussed in the literature [16]–[18], the state-space equations of the ac subsystem of the augmented system (3) are transformed to the rotating frame and

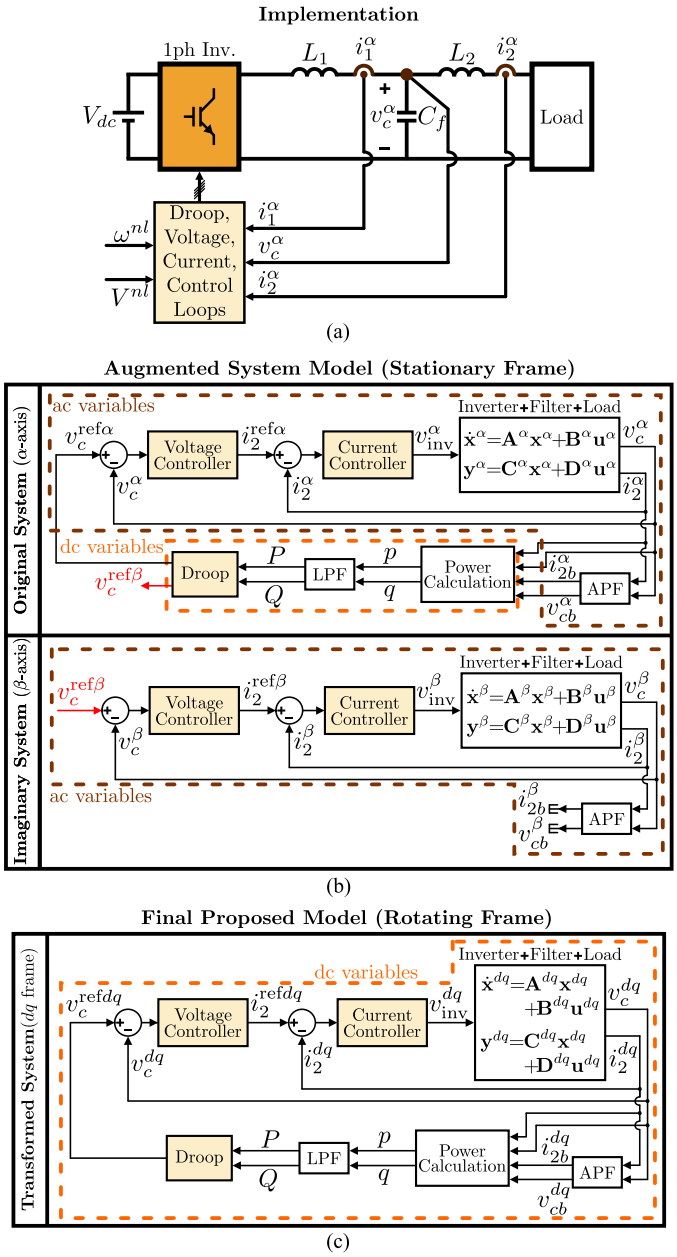

Fig. 4. Control system implementation and proposed modeling approach for a single-phase droop-controlled inverter. (a) Implementation. (b) Model containing the original, imaginary, and augmented systems in stationary frame. (c) Proposed large-signal (nonlinear) model containing the transformed system in rotating frame.

represented by

$$\dot{\mathbf{x}}^{dq}=\mathbf{A}^{dq}\mathbf{x}^{dq}+\mathbf{B}^{dq}\mathbf{u}^{dq},\ \mathbf{y}^{dq}=\mathbf{C}^{dq}\mathbf{x}^{dq}+\mathbf{D}^{dq}\mathbf{u}^{dq}$$
$$\mathbf{A}^{dq}=\begin{bmatrix}\mathbf{A} & \omega\mathbf{I}_{l_1}\\ -\omega\mathbf{I}_{l_1} & \mathbf{A}\end{bmatrix},\mathbf{B}^{dq}=\mathbf{B}^{\alpha\beta},\mathbf{C}^{dq}=\mathbf{C}^{\alpha\beta},\mathbf{D}^{dq}=\mathbf{D}^{\alpha\beta}\quad(4)$$

where $\mathbf{x}^{dq}=[\mathbf{x}^d\ \mathbf{x}^q]^T$, $\mathbf{y}^{dq}=[\mathbf{y}^d\ \mathbf{y}^q]^T$, and $\mathbf{u}^{dq}=[\mathbf{u}^d\ \mathbf{u}^q]^T$. Also, ω refers to the rotating speed of the frame. Observing (3) and (4), based on elementary rules of linear algebra, it is concluded that $\lambda(\mathbf{A}^{dq})=\lambda(\mathbf{A}^{\alpha\beta})\pm j\omega$ and $\lambda(\mathbf{A}^{\alpha\beta})=\lambda(\mathbf{A})$. Thus, the proposed approach does not alter the stability property, i.e., $\mathrm{Re}(\lambda(\mathbf{A}^{dq}))=\mathrm{Re}(\lambda(\mathbf{A}))$.

In summary, in the proposed modeling approach, the imaginary system (2) is defined the same as the ac subsystem of the original system (1) and excited by the quadrature signal u^β. Also, there is no feedback from the imaginary system to the original system. Therefore, the proposed modeling does not alter the stability properties of the original system. Moreover, the control system is designed and implemented in the stationary frame (without OSGs), and the imaginary system is only used for the system modeling and stability analysis. Thus, parameters' mismatch, which is a challenge in FAE method [8] and leads to steady-state errors in the orthogonal signals, does not have such a negative effect on the control system performance implemented in the stationary frame. This is further explained in Section VI.

The following algorithm summarizes the framework of the proposed approach. Details of how to run the algorithm are discussed subsequently.

A. *Proposed Step-by-Step Modeling Algorithm:*

Step 1: Derive state-space equations of the original system and classify them as*ac subsystem* and*dc subsystem*, as shown in Fig. 4(b).

Step 2: Consider the *ac subsystem* of the original system as α-axis system, i.e., (1).

Step 3: Define an imaginary system, β-axis system, the same as the system of *Step 2* excited by the quadrature signal, i.e., (2).

Step 4: Combine (1) and (2) to derive the state equations of the *ac subsystem* of the augmented system in the stationary frame, i.e., (3).

Step 5: Apply Park's transformation to (3) to derive the state equations of the *ac subsystem* of the augmented system in the rotating frame, i.e., (4), and combine them with the equations of the *dc subsystem* to find the large-signal (nonlinear) model in the rotating frame.

Step 6: The large-signal (nonlinear) model, which contains dc variables, is linearized at an operating point to find the small-signal (linearized) model, and the system stability is studied. The linearization process and operating point calculation are explained in the Appendix.

IV. Microgrid Equations in Stationary Frame

In this section, the entire state-space equations of the microgrid, shown in Fig. 1, including the parallel inverters and microgrid load are derived in the stationary frame. Also, as all inverters are in a parallel connection with each other, the state-space equations for one of the parallel inverters are derived in the following.

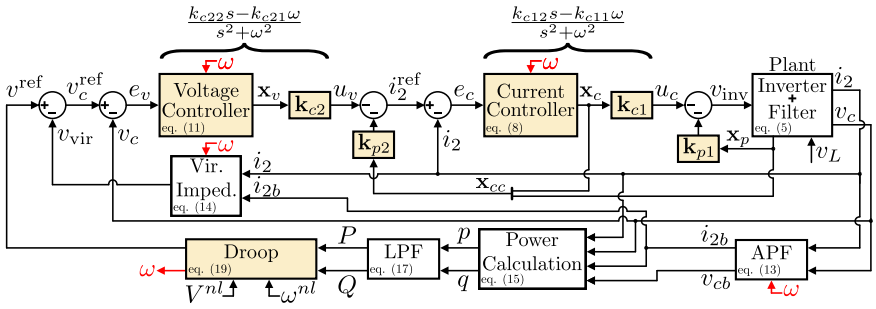

Fig. 5. Control loops of a droop-controlled inverter in the stationary frame.

A. Droop-Controlled Inverter Equations in Stationary Frame

The control system of a droop-controlled inverter contains three nested loops, which are the current, voltage, and droop-control loops, as shown in Fig. 5. In this figure, the current reference i_2^{ref} is determined internally by the voltage controller. In turn, the capacitor voltage tracks the voltage reference v_c^{ref} that is also determined by the droop controller [1], [19]. The two inner current and voltage control loops have only ac state variables, such as voltages, currents, and controllers' state variables. The droop-control loop introduces dc variables, such as the active and reactive powers. The droop control also contains nonlinear and trigonometric functions. Therefore, the entire system mixes both ac and dc variables and linear and nonlinear dynamics.

1) Current Control Loop: In a nested-loop control system, such as shown in Fig. 5, the current control loop is used to provide more flexibility in controlling and shaping the current dynamics and also current limitation in case a short circuit occurs [1], [19], and the loop is not for regulating or controlling the current independently. The state-space equations of the plant, containing the inverter and its *LCL* filter, are

$$\dot{\mathbf{x}}_p = \mathbf{A}_p\mathbf{x}_p + \mathbf{B}_p v_{\text{inv}} + \mathbf{B}_{pL}v_L,\ \mathbf{y}_p = \mathbf{C}_p\mathbf{x}_p \tag{5}$$

where $\mathbf{x}_p = [i_1\ v_c\ i_2]^T$ and $\mathbf{y}_p = [i_2\ v_c]^T$. Also, i_1, v_c, i_2, v_{inv}, and v_L refer to the current of the inverter-side inductor, the capacitor voltage, the current of the load-side inductor, the inverter voltage, and the load voltage, respectively. Moreover, $\mathbf{A}_p$, $\mathbf{B}_p$, $\mathbf{B}_{pL}$, and $\mathbf{C}_p$ are defined as follows:

$$c\mathbf{A}_p = \begin{bmatrix} 0 & \frac{-1}{L_1} & 0 \\ \frac{1}{C_f} & 0 & \frac{-1}{C_f} \\ 0 & \frac{1}{L_2} & 0 \end{bmatrix}, \mathbf{B}_p = \begin{bmatrix} \frac{1}{L_1} \\ 0 \\ 0 \end{bmatrix}, \mathbf{B}_{pL} = \begin{bmatrix} 0 \\ 0 \\ \frac{-1}{L_2} \end{bmatrix}$$

$$\mathbf{C}_p = \begin{bmatrix} \mathbf{C}_{p1}\ \mathbf{C}_{p2} \end{bmatrix}^T, \mathbf{C}_{p1} = \begin{bmatrix} 0\ 0\ 1 \end{bmatrix}, \mathbf{C}_{p2} = \begin{bmatrix} 0\ 1\ 0 \end{bmatrix} \tag{6}$$

where L_1, C_f, and L_2 denote the inverter-side inductance, capacitance, and the load-side inductance of the *LCL* filter, respectively.

As mentioned earlier, the voltage controller determines the current reference that can be either i_1^{ref} or i_2^{ref}. Since the quality of the output current is more important, the current loop is closed on i_2. Moreover, if a fault happens at the output terminal, limiting i_2 protects both the capacitor and inverter. In this article, a state feedback controller, which contains a resonant compensator to ensure sinusoidal reference tracking [20], is used, and its transfer function is as follows:

$$\frac{U_c}{E_c} = \frac{k_{c12}s - k_{c11}\omega}{s^2 + \omega^2} \tag{7}$$

where u_c is the resonant current controller effort, k_{c11} and k_{c12} are the controller parameters, and $e_c = i_2^{\text{ref}} - i_2$ is the current tracking error. Thus, the state-space equation of the current controller is

$$\begin{aligned} \dot{\mathbf{x}}_c &= \mathbf{A}_c\mathbf{x}_c + \mathbf{B}_c e_c \\ \mathbf{A}_c &= \begin{bmatrix} 0 & -\omega \\ \omega & 0 \end{bmatrix},\ \mathbf{B}_c = \begin{bmatrix} 0 \\ 1 \end{bmatrix} \end{aligned} \tag{8}$$

where $\mathbf{x}_c = [x_{c1}\ x_{c2}]^T$ is the state vector of the current controller, and ω is the operating angular frequency determined by the droop.

Considering $v_{\text{inv}} = -\mathbf{k}_{c1}\mathbf{x}_c - \mathbf{k}_{p1}\mathbf{x}_p$ where $\mathbf{k}_{c1} = [k_{c11}\ k_{c12}]$ and $\mathbf{k}_{p1} = [k_{p11}\ \cdots\ k_{p13}]$, (5)–(8) form the state-space equations of the current control loop as

$$\begin{aligned} &\dot{\mathbf{x}}_{cc} = \mathbf{A}_{cc}\mathbf{x}_{cc} + \mathbf{B}_{cc}i_2^{\text{ref}} + \mathbf{B}_{cL}v_L,\ y_{cc} = \mathbf{C}_{cc}\mathbf{x}_{cc} \\ &\mathbf{A}_{cc} = \begin{bmatrix} \mathbf{A}_c & -\mathbf{B}_c\mathbf{C}_{p1} \\ -\mathbf{B}_p\mathbf{k}_{c1} & \mathbf{A}_p - \mathbf{B}_p\mathbf{k}_{p1} \end{bmatrix} \\ &\mathbf{B}_{cc} = \begin{bmatrix} \mathbf{B}_c \\ \mathbf{0}_{3\times 1} \end{bmatrix}, \mathbf{B}_{cL} = \begin{bmatrix} \mathbf{0}_{2\times 1} \\ \mathbf{B}_{pL} \end{bmatrix}, \mathbf{C}_{cc} = \begin{bmatrix} \mathbf{0}_{1\times 2}\ \mathbf{C}_{p2} \end{bmatrix} \end{aligned} \tag{9}$$

where $\mathbf{x}_{cc} = [\mathbf{x}_c\ \mathbf{x}_p]^T$ and $y_{cc} = v_c$. The gain vectors $\mathbf{k}_{c1}$ and $\mathbf{k}_{p1}$ of the state feedback controller are optimally designed using the LQT method [20].

2) Voltage Control Loop: The voltage control loop is also shown in Fig. 5. The voltage controller is also a state feedback controller, comprising a resonant compensator to ensure sinusoidal reference tracking, with the following transfer function

$$\frac{U_v}{E_v} = \frac{k_{c22}s - k_{c21}\omega}{s^2 + \omega^2} \tag{10}$$

where u_v is the resonant voltage controller effort, k_{c21} and k_{c22} are the controller parameters, and $e_v = v_c^{\text{ref}} - v_c$ denotes the voltage error. Also, the state-space equation of the voltage controller is

$$\dot{\mathbf{x}}_v = \mathbf{A}_v\mathbf{x}_v + \mathbf{B}_v e_v \tag{11}$$

where $\mathbf{x}_v = [x_{v1}\ x_{v2}]^T$ is the state vector of the voltage controller. Also, $\mathbf{A}_v$ and $\mathbf{B}_v$ are equal to $\mathbf{A}_c$ and $\mathbf{B}_c$ in (8), respectively.

Using $i_2^{\text{ref}} = -\mathbf{k}_{c2}\mathbf{x}_v - \mathbf{k}_{p2}\mathbf{x}_{cc}$ where $\mathbf{k}_{c2} = [k_{c21}\ k_{c22}]$ and $\mathbf{k}_{p2} = [k_{p21}\ \cdots\ k_{p25}]$, the state-space equations of the resonant controller (11) and the current control loop (9) are augmented to derive the voltage control-loop equations

$$\dot{\mathbf{x}}_{vc} = \mathbf{A}_{vc}\mathbf{x}_{vc} + \mathbf{B}_{vc}v_c^{\text{ref}} + \mathbf{B}_{vL}v_L,\ \mathbf{y}_{vc} = \mathbf{C}_{vc}\mathbf{x}_{vc}$$
$$\mathbf{A}_{vc} = \begin{bmatrix} \mathbf{A}_v & -\mathbf{B}_v\mathbf{C}_{cc} \\ -\mathbf{B}_{cc}\mathbf{k}_{c2} & \mathbf{A}_{cc} - \mathbf{B}_{cc}\mathbf{k}_{p2} \end{bmatrix}$$
$$\mathbf{B}_{vc} = \begin{bmatrix} \mathbf{B}_v \\ \mathbf{0}_{5\times 1} \end{bmatrix}, \mathbf{B}_{vL} = \begin{bmatrix} \mathbf{0}_{2\times 1} \\ \mathbf{B}_{cL} \end{bmatrix}, \mathbf{C}_{vc} = \begin{bmatrix} \mathbf{0}_{2\times 4}\ \mathbf{C}_p \end{bmatrix} \quad (12)$$

where $\mathbf{x}_{vc} = [\mathbf{x}_v\ \mathbf{x}_{cc}]^T$ and $\mathbf{y}_{vc} = \mathbf{y}_p$. Also, the gain vectors $\mathbf{k}_{c2}$ and $\mathbf{k}_{p2}$ of the state feedback controller are optimally designed using the LQT method [20].

3) Droop Control Loop: The droop-control loop consists of the voltage control loop, all-pass filters (APFs), virtual impedance, power calculation block, low-pass filters (LPFs), and droop characteristics, as shown in Fig. 5.

APF block: First-order APFs are used to introduce 90° phase-shift. The state-space equations of the APFs are

$$\dot{\mathbf{x}}_{ap} = \mathbf{A}_{ap}\mathbf{x}_{ap} + \mathbf{B}_{ap}\mathbf{u}_{ap},\ \mathbf{y}_{ap} = \mathbf{C}_{ap}\mathbf{x}_{ap} + \mathbf{D}_{ap}\mathbf{u}_{ap}$$
$$\mathbf{A}_{ap} = -\omega\mathbf{I}_2,\ \mathbf{B}_{ap} = \omega\mathbf{I}_2,\ \mathbf{C}_{ap} = 2\mathbf{I}_2, \mathbf{D}_{ap} = -\mathbf{I}_2 \quad (13)$$

where $\mathbf{x}_{ap}$ is the state vector of the APFs, $\mathbf{u}_{ap} = [i_2\ v_c]^T$, $\mathbf{y}_{ap} = [i_{2b}\ v_{cb}]^T$, and $\mathbf{I}_2$ is the identity matrix of dimension 2.

4) Virtual Impedance Block: An RL virtual impedance, $G_{\text{vir}} = R_{\text{vir}} + L_{\text{vir}}s$, is used to fix the output impedance of the inverter and to improve the stability of parallel inverters [21], [22]. Considering i_2 and v_{vir} as the input and output of this block, respectively, the voltage drop across the virtual impedance is $v_{\text{vir}} = R_{\text{vir}}i_2 + L_{\text{vir}}\frac{di_2}{dt}$. For a sinusoidal signal with the angular frequency ω, the derivative term can be approximated as $\frac{d(i_2)}{dt} = -\omega i_{2b}$, where i_{2b} is the 90° phase-shifted signal of i_2 and is generated by the APF. Therefore, the virtual impedance equation is rewritten as

$$y_{\text{vir}} = \mathbf{D}_{\text{vir}}\mathbf{u}_{\text{vir}},\ \mathbf{D}_{\text{vir}} = \begin{bmatrix} R_{\text{vir}} & -L_{\text{vir}}\omega \end{bmatrix} \quad (14)$$

where $\mathbf{u}_{\text{vir}} = [i_2\ i_{2b}]^T$ and $y_{\text{vir}} = v_{\text{vir}}$.

5) Power Calculation Block: It calculates the instantaneous active and reactive powers, and its equation is given by

$$\mathbf{y}_{pq} = \mathbf{f}_{pq}(\mathbf{u}_{pq}),\ \mathbf{f}_{pq} = \begin{bmatrix} f_p\ f_q \end{bmatrix}^T \quad (15)$$

where $\mathbf{u}_{pq} = [i_2\ i_{2b}\ v_c\ v_{cb}]^T$ and $\mathbf{y}_{pq} = [p\ q]^T$. Also, power calculation functions f_p and f_q are

$$f_p = 0.5\left(v_c i_2 + v_{cb} i_{2b}\right),\ f_q = 0.5\left(v_{cb} i_2 - v_c i_{2b}\right). \quad (16)$$

This block adds nonlinear dynamics to the system.

6) LPF Block: LPFs are used for the power measurement to smooth down active and reactive power characteristics. Also, LPFs give an inertia-type behavior to the inverter [23]. For first-order LPFs with the transfer function $G_{lp}(s) = \frac{1}{\tau_{lp}s+1}$, where τ_{lp} is the time-constant of the LPFs, the state-space equations are

$$\begin{aligned} &\dot{\mathbf{x}}_{lp} = \mathbf{A}_{lp}\mathbf{x}_{lp} + \mathbf{B}_{lp}\mathbf{u}_{lp},\ \mathbf{y}_{lp} = \mathbf{C}_{lp}\mathbf{x}_{lp} \\ &\mathbf{A}_{lp} = \tfrac{-1}{\tau_{lp}}\mathbf{I}_2,\ \mathbf{B}_{lp} = \tfrac{1}{\tau_{lp}}\mathbf{I}_2,\ \mathbf{C}_{lp} = \mathbf{I}_2 \end{aligned} \quad (17)$$

where $\mathbf{u}_{lp} = [p\ q]^T$ and $\mathbf{x}_{lp} = \mathbf{y}_{lp} = [P\ Q]^T$.

Droop block: Droop characteristics are expressed by

$$\begin{aligned} &\dot{\phi} = \omega,\ v^{\text{ref}} = V\cos\phi \\ &\omega = \omega^{nl} - m_p P,\ V = V^{nl} - m_q Q \end{aligned} \quad (18)$$

where ω, V, and ϕ refer to the angular frequency, amplitude, and angle of the reference voltage v^{ref}. Also, m_p and m_q are the droop coefficients. ω^{nl} and V^{nl} denote the no-load angular frequency and amplitude of the no-load voltage, respectively, and they are determined by the higher control level, known as secondary control, which is not discussed in this article. Therefore, to form the standard state-space equation of the droop controller as $\dot{x}_d = \mathbf{A}_d x_d + \mathbf{B}_d\mathbf{u}_d$, the input of the droop controller $\mathbf{u}_d$ is considered as $\mathbf{u}_d = [P\ Q\ \omega^{nl}\ V^{nl}]^T$. Consequently, the equations of the droop controller (18) can be rewritten as

$$\begin{aligned} &\dot{x}_d = \mathbf{A}_d x_d + \mathbf{B}_d\mathbf{u}_d \\ &\mathbf{y}_d = \begin{bmatrix} f_d(x_d, \mathbf{u}_d) & \mathbf{C}_{2d}x_d + \mathbf{D}_{2d}\mathbf{u}_d \end{bmatrix}^T \\ &\mathbf{A}_d = \mathbf{C}_{2d} = 0,\ \mathbf{B}_d = \mathbf{D}_{2d}\begin{bmatrix} -m_p & 0 & 1 & 0 \end{bmatrix} \end{aligned} \quad (19)$$

where $x_d = \phi$, $\mathbf{y}_d = [v^{\text{ref}}\ \omega]^T$, and $f_d = (V^{nl} - m_q Q)\cos\phi$. The droop loop introduces dc state variables, such as the active and reactive powers, and also nonlinear and trigonometric terms.

B. Microgrid Load Equations in Stationary Frame

It is assumed that the microgrid load is a combination of series resistive R, inductive L, and capacitive C components. Therefore, the load voltage can be calculated as $v_L = Ri_L + L\frac{di_L}{dt} + v_{c_L}$. The capacitive component C introduces a new state variable as $\dot{v}_{c_L} = \frac{1}{C}i_L$, where v_{c_L} and i_L are the capacitive part of the load voltage and the current, respectively. According to $i_L = \sum_{n=1}^{N} i_{2,n}$ and $\frac{di_{2,n}}{dt} = \frac{v_{c,n} - v_L}{L_{2,n}}$, the load voltage is written as

$$v_L = \frac{R\sum_{n=1}^{N} i_{2,n} + L\sum_{n=1}^{N}\frac{v_{c,n}}{L_{2,n}} + v_{c_L}}{\Lambda} \quad (20)$$

where $\Lambda = 1 + L\sum_{n=1}^{N}\frac{1}{L_{2,n}}$. Hereinafter, the indices "$,n$" and "n" refer to signals, variables, and components of the nth inverter. The state-space equations of the microgrid load are

$$\begin{aligned} &\dot{x}_L = \mathbf{B}_L\mathbf{u}_L, y_L = \mathbf{C}_L x_L + \mathbf{D}_L\mathbf{u}_L \\ &\mathbf{B}_L = \frac{1}{C}\text{ones}(1, 2\text{˜}N),\ \mathbf{C}_L = \begin{bmatrix} \frac{1}{\Lambda} \end{bmatrix} \\ &\mathbf{D}_L = \frac{\begin{bmatrix} R\times\text{ones}(1,N)\ \frac{L}{L_{2,1}}\ \cdots\ \frac{L}{L_{2,N}} \end{bmatrix}}{\Lambda} \end{aligned} \quad (21)$$

where $\mathbf{u}_L = [i_{2,1}\ \cdots\ i_{2,N}\ v_{c,1}\ \cdots\ v_{c,N}]^T$, $x_L = v_{c_L}$, and $y_L = v_L$.

To sum up, in this section, the state-space equations of the microgrid, shown in Fig. 1, are derived in the stationary frame. Therefore, in Section V, an imaginary-twin system is defined with respect to (5)–(21) to generate required signals for Park's transformation without adding any OSGs.

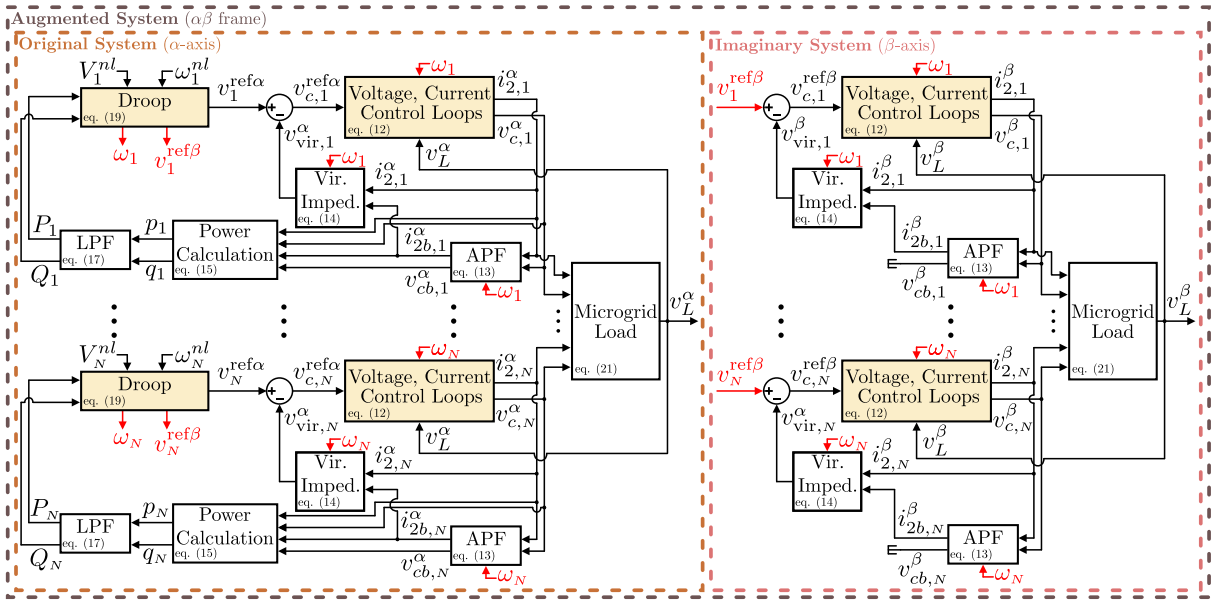

Fig. 6. Control block diagrams of the original, imaginary, and augmented systems for N parallel inverters in stationary frame.

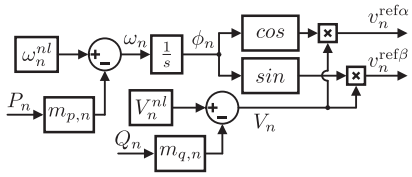

Fig. 7. Droop configuration of the nth inverter.

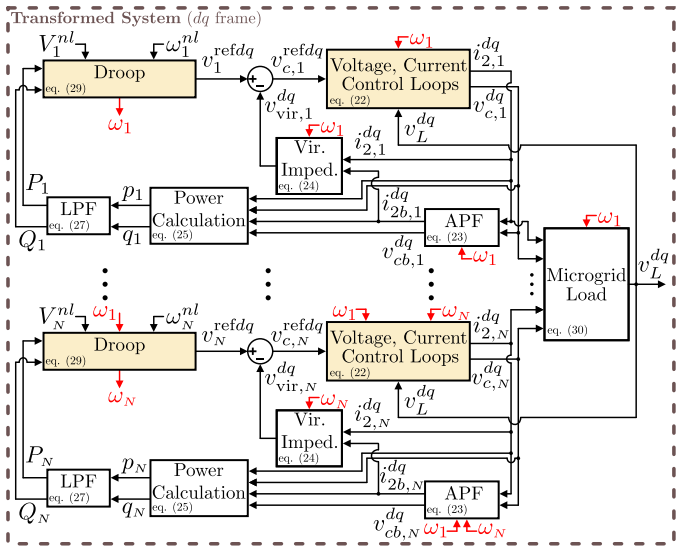

Fig. 8. Proposed large-signal (nonlinear) model of the microgrid containing N parallel inverters in the rotating frame.

V. Microgrid Equations in Rotating Frame

A. Proposed Approach Implementation

According to the proposed modeling algorithm in Section III, first, all state equations of the original system, derived in Section IV, are considered to form the α-axis system (*Step 1* and *Step 2*). Then, the imaginary system, β-axis system, is defined accordingly (*Step 3*). In this case, the state-space equations containing ac variables in Section IV, i.e., (5)–(14) and (21), are valid for the imaginary system as well. Also, as the inputs of the imaginary system $v_n^{\text{ref}\beta}$ and the ac subsystem of the original system $v_n^{\text{ref}\alpha}$ are orthogonal, their variables are orthogonal as well. Now, the original and imaginary systems are combined to form the augmented system in the stationary frame, as shown in Fig. 6 (*Step 4*). Next, the equations of the augmented system are converted to the rotating frame to derive the proposed large-signal (nonlinear) model, as shown in Fig. 8 (*Step 5*). Finally, the large-signal (nonlinear) model is linearized at an operating point to find the proposed small-signal (linearized) model to be used for small-signal analysis (*Step 6*).

In systems containing multiple inverters, to derive the system model in *dq-frame* , it is common that one of the inverters' frames, whose angles are indicated by ϕ_n, is considered as the reference frame, and all variables are transformed to that frame using the Park's transformation. In this article, the first inverter's frame, whose angle is ϕ_1 and rotates with the angular frequency $\omega_1 = \frac{d\phi_1}{dt}$, is considered as the reference frame. It is worth mentioning that no special treatment is considered for Inverter 1, and the inverter's frame selection as the reference frame is arbitrary.

B. Droop-Controlled Inverter Equations in Rotating Frame

In the following, the equations of the nth droop-controlled inverter (12)–(19) are transformed to the rotating frame using the equation derived for the transformation (4) [16].

TABLE I
NOMINAL SYSTEM PARAMETERS OF MICROGRID

Inverter 1		Inverter 2	
Parameter	Value	Parameter	Value
P_1^{nom}	1 kW	P_2^{nom}	2 kW
$L_{1,1}$	2 mH	$L_{1,2}$	3 mH
$C_{f,1}$	2.2 μF	$C_{f,2}$	1 μF
$L_{2,1}$	2 mH	$L_{2,2}$	2 mH
$L_{\text{vir},1}$	2 mH	$L_{\text{vir},2}$	2 mH
$R_{\text{vir},1}$	0.1Ω	$R_{\text{vir},2}$	0.1Ω
$\tau_{lp,1}$	$\frac{1}{2\pi 10}s$	$\tau_{lp,2}$	$\frac{1}{2\pi 10}s$
ω_1^{nl}	$2\pi 60.5\frac{\text{rad}}{s}$	ω_2^{nl}	$2\pi 60.5\frac{\text{rad}}{s}$
V_1^{nl}	170 V	V_2^{nl}	170 V
$m_{p,1}$	$\frac{2\pi}{1000}$	$m_{p,2}$	$\frac{2\pi}{2000}$
$m_{q,1}$	0.01	$m_{q,2}$	0.005

TABLE II
PARAMETERS OF CURRENT AND VOLTAGE CONTROLLERS

	Inverter 1		Inverter 2	
	Parameter	Value	Parameter	Value
Current Controller	$k_{c11,1}$	8.17×10^4	$k_{c11,2}$	8.05×10^4
	$k_{c12,1}$	-3.89×10^4	$k_{c12,2}$	-4.07×10^4
	$k_{p11,1}$	20.58	$k_{p11,2}$	31.63
	$k_{p12,1}$	0.13	$k_{p12,2}$	0.11
	$k_{p13,1}$	-0.82	$k_{p13,2}$	-8.63
Voltage Controller	$k_{c21,1}$	174	$k_{c21,2}$	164
	$k_{c22,1}$	-162	$k_{c22,2}$	-172
	$k_{p21,1}$	-4.36×10^3	$k_{p21,2}$	-3.38×10^3
	$k_{p22,1}$	2.75×10^3	$k_{p22,2}$	2.23×10^3
	$k_{p23,1}$	0.09	$k_{p23,2}$	0.07
	$k_{p24,1}$	6.9×10^{-3}	$k_{p24,2}$	1.9×10^{-3}
	$k_{p25,1}$	-0.22	$k_{p25,2}$	-0.31

Regarding the voltage and current control loops of the nth inverter, (12), which contains both loops dynamics, is written in the rotating frame as

$$\dot{\mathbf{x}}_{vc,n}^{dq}=\mathbf{A}_{vc,n}^{dq}\mathbf{x}_{vc,n}^{dq}+\mathbf{B}_{vc,n}^{dq}v_{c,n}^{\text{ref}dq}+\mathbf{B}_{vL,n}^{dq}v_L^{dq}$$
$$\mathbf{y}_{vc,n}^{dq}=\mathbf{C}_{vc,n}^{dq}\mathbf{x}_{vc,n}^{dq}$$
$$\mathbf{A}_{vc,n}^{dq}=\begin{bmatrix}\mathbf{A}_{vc,n} & \omega_1\mathbf{I}_7\\ -\omega_1\mathbf{I}_7 & \mathbf{A}_{vc,n}\end{bmatrix},\mathbf{B}_{vc,n}^{dq}=\begin{bmatrix}\mathbf{B}_{vc,n} & \mathbf{0}_{7\times1}\\ \mathbf{0}_{7\times1} & \mathbf{B}_{vc,n}\end{bmatrix}$$
$$\mathbf{B}_{vL,n}^{dq}=\begin{bmatrix}\mathbf{B}_{vL,n} & \mathbf{0}_{7\times1}\\ \mathbf{0}_{7\times1} & \mathbf{B}_{vL,n}\end{bmatrix},\mathbf{C}_{vc,n}^{dq}=\begin{bmatrix}\mathbf{C}_{vc,n} & \mathbf{0}_{2\times7}\\ \mathbf{0}_{2\times7} & \mathbf{C}_{vc,n}\end{bmatrix} \quad (22)$$

where $\mathbf{x}_{vc,n}^{dq}=[\mathbf{x}_{v,n}^d\ \ \mathbf{x}_{cc,n}^d\ \ \mathbf{x}_{v,n}^q\ \ \mathbf{x}_{cc,n}^q]^T$ and $\mathbf{y}_{vc,n}^{dq}=[i_{2,n}^d\ v_{c,n}^d\ i_{2,n}^q\ v_{c,n}^q]^T$. Also, $\mathbf{x}_{cc,n}^{dq}=[\mathbf{x}_{c,n}^d\ \mathbf{x}_{p,n}^d\ \mathbf{x}_{c,n}^q\ \mathbf{x}_{p,n}^q]^T$ and $\mathbf{x}_{p,n}^{dq}=[i_{1,n}^d\ v_{c,n}^d\ i_{2,n}^d\ i_{1,n}^q\ v_{c,n}^q\ i_{2,n}^d]^T$.

The next step is to transform the state-space equations of the droop loop to the rotating frame. Considering the state-space equations of APFs (13), the transformed equations are

$$\dot{\mathbf{x}}_{ap,n}^{dq}=\mathbf{A}_{ap,n}^{dq}\mathbf{x}_{ap,n}^{dq}+\mathbf{B}_{ap,n}^{dq}\mathbf{u}_{ap,n}^{dq}$$
$$\mathbf{y}_{ap,n}^{dq}=\mathbf{C}_{ap,n}^{dq}\mathbf{x}_{ap,n}^{dq}+\mathbf{D}_{ap,n}^{dq}\mathbf{u}_{ap,n}^{dq}$$

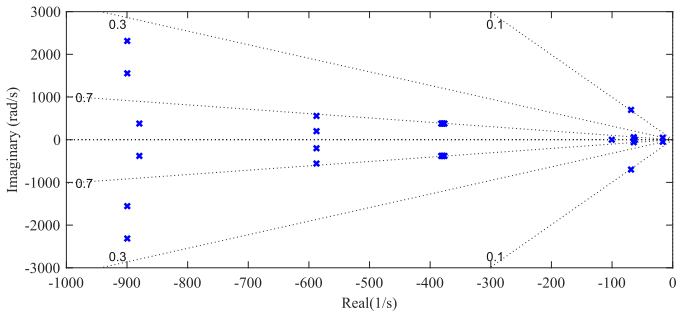

Fig. 9. Dominant poles of the system consisting of droop-controlled inverters obtained from the proposed small-signal (linearized) model.

TABLE III
TRANSFER FUNCTIONS OF CONVENTIONAL OSG METHODS

Hilbert Transform	SOGI
$G_h(s)=\frac{\omega_b-s}{\omega_b+s}$	$G_\alpha(s)=\frac{k_d\omega_b s}{s^2+k_d\omega_b s+\omega_b^2}$ $G_\beta(s)=\frac{k_d\omega_b^2}{s^2+k_d\omega_b s+\omega_b^2}$

Note: ω_b: Angular frequency. k_d: Damping factor ($k_d=0.7$).

$$\mathbf{A}_{ap,n}^{dq}=\begin{bmatrix}\mathbf{A}_{ap,n} & \omega_1\mathbf{I}_2\\ -\omega_1\mathbf{I}_2 & \mathbf{A}_{ap,n}\end{bmatrix},\mathbf{B}_{ap,n}^{dq}=\begin{bmatrix}\mathbf{B}_{ap,n} & \mathbf{0}_{2\times2}\\ \mathbf{0}_{2\times2} & \mathbf{B}_{ap,n}\end{bmatrix}$$
$$\mathbf{C}_{ap,n}^{dq}=\begin{bmatrix}\mathbf{C}_{ap,n} & \mathbf{0}_{2\times2}\\ \mathbf{0}_{2\times2} & \mathbf{C}_{ap,n}\end{bmatrix},\mathbf{D}_{ap,n}^{dq}=\begin{bmatrix}\mathbf{D}_{ap,n} & \mathbf{0}_{2\times2}\\ \mathbf{0}_{2\times2} & \mathbf{D}_{ap,n}\end{bmatrix} \quad (23)$$

where

$$\mathbf{u}_{ap,n}^{dq}=[i_{2,n}^d\ v_{c,n}^d\ i_{2,n}^q\ v_{c,n}^q]^T,\ \mathbf{y}_{ap,n}^{dq}=\left[i_{2b,n}^d\ v_{cb,n}^d\ i_{2b,n}^q\ v_{cb,n}^q\right]^T.$$

Considering (14), the transformed equation of the virtual impedance block in the rotating frame is

$$\mathbf{y}_{\text{vir},n}^{dq}=\mathbf{D}_{\text{vir},n}^{dq}\mathbf{u}_{\text{vir},n}^{dq},\ \mathbf{D}_{\text{vir},n}^{dq}=\begin{bmatrix}\mathbf{D}_{\text{vir},n} & \mathbf{0}_{1\times2}\\ \mathbf{0}_{1\times2} & \mathbf{D}_{\text{vir},n}\end{bmatrix} \quad (24)$$

where

$$\mathbf{u}_{\text{vir},n}^{dq}=\left[i_{2,n}^d\ i_{2b,n}^d\ i_{2,n}^q\ i_{2b,n}^q\right]^T,\ \mathbf{y}_{\text{vir},n}^{dq}=[v_{\text{vir},n}^d\ v_{\text{vir},n}^q]^T.$$

As for the power calculation block, (15) can be rewritten based on the rotating frame variables as

$$\mathbf{y}_{pq,n}=\mathbf{g}_{pq,n}(\mathbf{u}_{pq,n}^{dq}),\ \mathbf{g}_{pq,n}=\left[\,g_{p,n}\ g_{q,n}\,\right]^T \quad (25)$$

where $\mathbf{u}_{pq,n}^{dq}=[i_{2,n}^{dq}\ i_{2b,n}^{dq}\ v_{c,n}^{dq}\ v_{cb,n}^{dq}]^T$, $\mathbf{y}_{pq,n}=[p_n\ q_n]^T$ and

$$g_{p,n}=0.25\left(v_{c,n}^d i_{2,n}^d+v_{c,n}^q i_{2,n}^q+v_{cb,n}^d i_{2b,n}^d+v_{cb,n}^q i_{2b,n}^q\right)$$
$$g_{q,n}=0.25\left(v_{cb,n}^d i_{2,n}^d+v_{cb,n}^q i_{2,n}^q-v_{c,n}^d i_{2b,n}^d-v_{c,n}^q i_{2b,n}^q\right). \quad (26)$$

For the LPF block of the nth inverter, (17) is rewritten as

$$\dot{\mathbf{x}}_{lp,n}=\mathbf{A}_{lp,n}\mathbf{x}_{lp,n}+\mathbf{B}_{lp,n}\mathbf{u}_{lp,n},\ \mathbf{y}_{lp,n}=\mathbf{C}_{lp,n}\mathbf{x}_{lp,n} \quad (27)$$

where $\mathbf{u}_{lp,n}=[p_n\ q_n]^T$ and $\mathbf{x}_{lp,n}=\mathbf{y}_{lp,n}=[P_n\ Q_n]^T$.

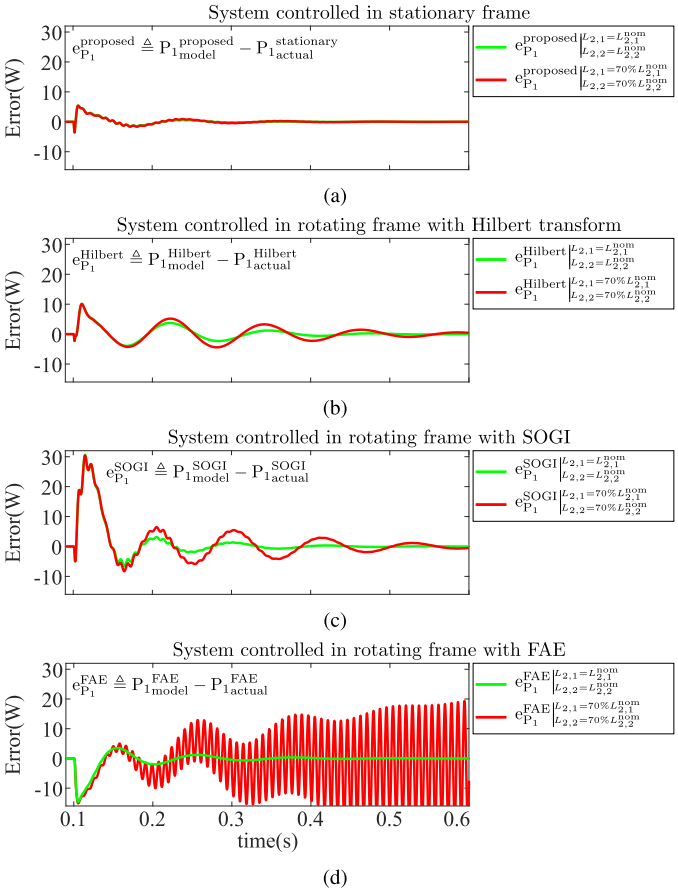

Fig. 10. Large-signal model prediction errors and robustness against load-side inductance $L_{2,1}, L_{2,2}$ variations.

Fig. 7 shows the droop block diagram that illustrates how the reference signals are generated for the original system $v_n^{\text{ref}\alpha} = V_n \cos\phi_n$ and the imaginary system $v_n^{\text{ref}\beta} = V_n \sin\phi_n$. Thus, the transformed reference signals generated by the droop block in the first inverter's rotating frame are

$$v_n^{\text{ref}d} = V_n \cos(\phi_n - \phi_1),\ v_n^{\text{ref}q} = V_n \sin(\phi_n - \phi_1). \quad (28)$$

In Fig. 7, ϕ_n is the state of the droop block, which is a ramp function. Therefore, it is not proper for the system linearization and finding the operating point. To resolve this issue, according to (28), a new state variable $z_{d,n}$ is defined for the droop block as $z_{d,n} = \phi_n - \phi_1$. In this case, although both ϕ_n and ϕ_1 are ramp functions, their difference $z_{d,n}$ is a dc variable. According to the new variable definition and (18), the droop characteristics of the nth inverter in the rotating frame are

$$\begin{aligned} \dot{z}_{d,n} &= \dot{\phi}_n - \dot{\phi}_1 = \omega_n^{nl} - m_{p,n}P_n - \omega_1 \\ v_n^{\text{ref}d} &= V_n \cos z_{d,n},\ v_n^{\text{ref}q} = V_n \sin z_{d,n} \\ \omega_n &= \omega_n^{nl} - m_{p,n}P_n,\ V_n = V_n^{nl} - m_{q,n}Q_n. \end{aligned} \quad (29)$$

Therefore, according to (19) and (29), the state-space equations of the droop characteristics in the rotating frame are

$$\dot{z}_{d,n} = \mathbf{B}_{d,n}^{dq}\mathbf{u}_{d,n}^{dq},\ \mathbf{y}_{d,n}^{dq} = \left[\mathbf{g}_d(z_{d,n}, \mathbf{u}_{d,n}^{dq})\ \mathbf{D}_{3\,d,n}\mathbf{u}_{d,n}^{dq}\right]^T$$

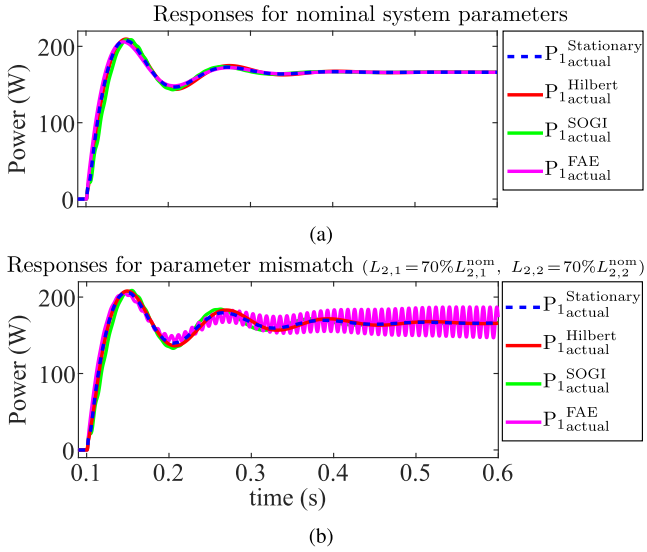

Fig. 11. Active power injections of the first inverter controlled either in the stationary or rotating frame (*Scenario-I*).

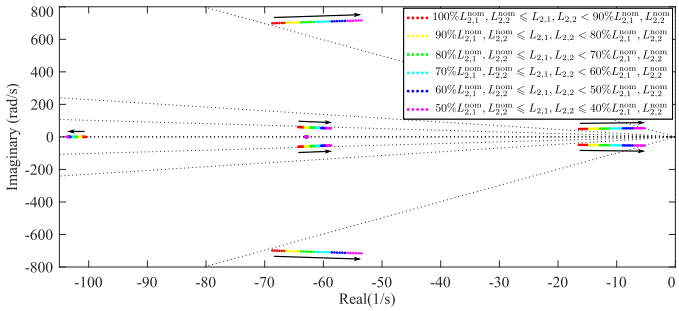

Fig. 12. Dominant pole variations due to the drop of $L_{2,1}$ and $L_{2,2}$ to 40% of their nominal values obtained from the proposed small-signal (linearized) model.

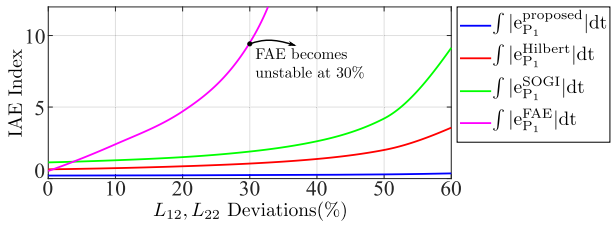

Fig. 13. IAE of large-signal models.

$$\mathbf{B}_{d,n}^{dq} = \left[\mathbf{B}_{d,n}\ -1\right],\ \mathbf{D}_{3\,d,n}^{dq} = \left[\mathbf{D}_{2\,d,n}\ 0\right] \quad (30)$$

where $\mathbf{u}_{d,n}^{dq} = [\mathbf{u}_{d,n}\ \omega_1]^T$, $\mathbf{y}_{d,n}^{dq} = [v_n^{\text{ref}d}\ v_n^{\text{ref}q}\ \omega_n]^T$, and $\mathbf{g}_d = [(V_n^{nl} - m_{q,n}Q_n)\cos z_{d,n}\ (V_n^{nl} - m_{q,n}Q_n)\sin z_{d,n}]^T$.

It is worth mentioning that, according to the definition of $z_{d,n}$, the new droop state of the first inverter would be $z_{d,1} = \phi_1 - \phi_1 = 0$, which means that $z_{d,1}$ is always zero and it does not appear in state-space equations of the microgrid in the rotating frame. This is due to the fact that all equations are transformed to the first inverter's rotating frame.

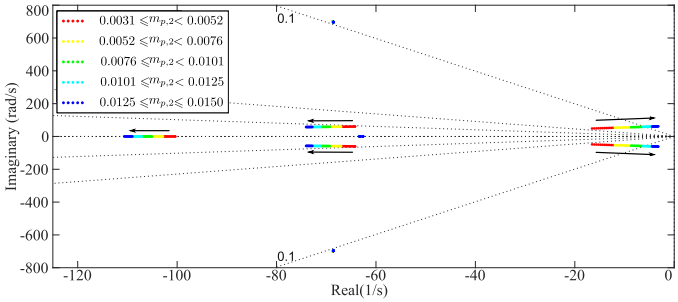

Fig. 14. Dominant pole variations due to $m_{p,2}$ changes to have a marginal stability operating mode obtained from the proposed small-signal (linearized) model.

C. Microgrid Load Equations in Rotating Frame

Using the proposed method, the state-space equations of the microgrid load in the rotating frame are

$$\dot{\mathbf{x}}_L^{dq} = \mathbf{A}_L^{dq}\mathbf{x}_L^{dq} + \mathbf{B}_L^{dq}\mathbf{u}_L^{dq},\ \mathbf{y}_L^{dq} = \mathbf{C}_L^{dq}\mathbf{x}_L^{dq} + \mathbf{D}_L^{dq}\mathbf{u}_L^{dq}$$
$$\mathbf{A}_L^{dq} = \begin{bmatrix} 0 & \omega_1 \\ -\omega_1 & 0 \end{bmatrix}, \mathbf{B}_L^{dq} = \begin{bmatrix} \mathbf{B}_L & \mathbf{0}_{1\times 2N} \\ \mathbf{0}_{1\times 2N} & \mathbf{B}_L \end{bmatrix}$$
$$\mathbf{C}_L^{dq} = \begin{bmatrix} \mathbf{C}_L & 0 \\ 0 & \mathbf{C}_L \end{bmatrix}, \mathbf{D}_L^{dq} = \begin{bmatrix} \mathbf{D}_L & \mathbf{0}_{1\times 2N} \\ \mathbf{0}_{1\times 2N} & \mathbf{D}_L \end{bmatrix} \quad (31)$$

where $\mathbf{x}_L^{dq}=[v_{c_L}^d \quad v_{c_L}^q]^T$, $\mathbf{y}_L^{dq}=[v_L^d \quad v_L^q]^T$, and $\mathbf{u}_L^{dq}=[i_{2,1}^d \cdots i_{2,N}^d \ v_{c,1}^d \cdots v_{c,N}^d \ i_{2,1}^q \cdots i_{2,N}^q \ v_{c,1}^q \cdots v_{c,N}^q]^T$.

Finally, based on (22)–(31), Fig. 6, which illustrates the microgrid model, including the original, imaginary, and augmented systems in the stationary frame, can be redrawn, as shown in Fig. 8. This figure shows the large-signal (nonlinear) model of the single-phase microgrid in the rotating frame based on the proposed approach. This model only contains dc variables; thus, by linearizing it at an operating point, the stability analysis of the microgrid and the parameter sensitivity can be studied as explained in Section VI.

Furthermore, according to Figs. 6 and 8, it is observed that, for N parallel inverters, the total number of state variables of the transformed system equals $21N + 1$. On the other hand, the number of state variables of the original system is equal to $12N + 1$. Although the proposed method for modeling a single-phase microgrid, controlled in the stationary frame, increases the order of the entire system, the transformation does not affect dynamics and stability properties of the original system as discussed in Section III.

VI. Stability Analysis and Model Verification

In this section, the microgrid stability analysis is addressed using small-signal (linearized) equations that are derived by linearizing the large-signal model at an operating point as explained in the Appendix. Then, the accuracy of the proposed modeling approach is verified and compared with existing approaches.

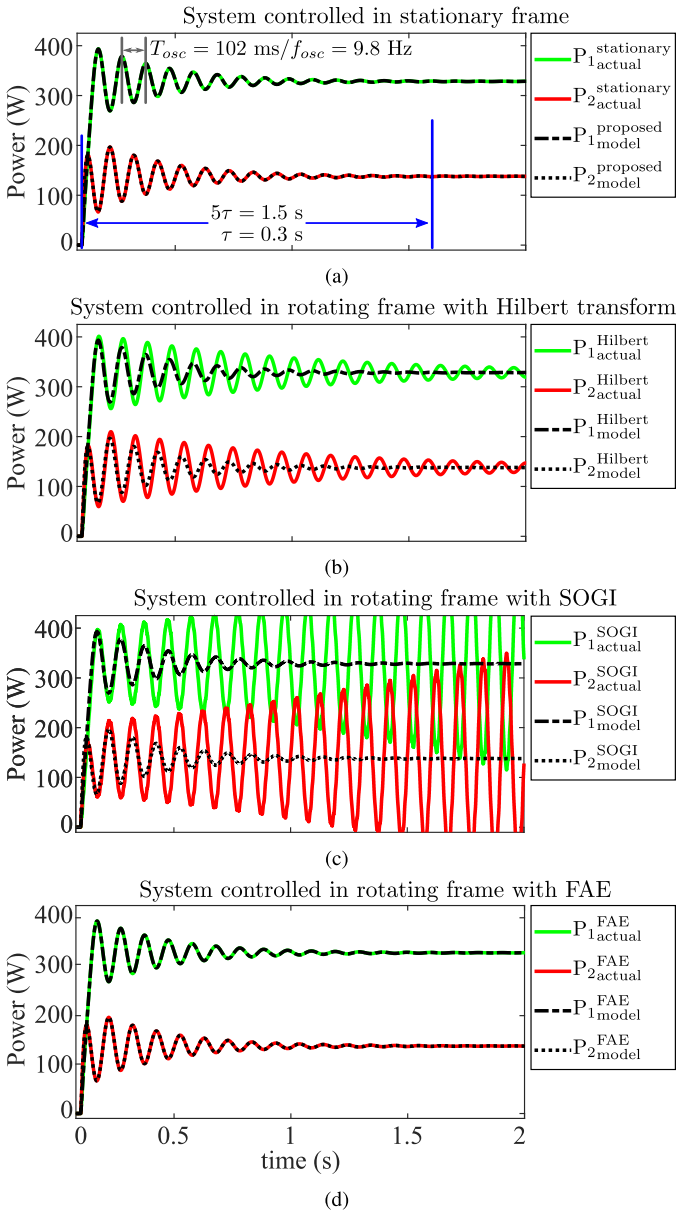

Fig. 15. Active power injection responses for actual systems, controlled in either the stationary or rotating frame, and their large-signal model predictions.

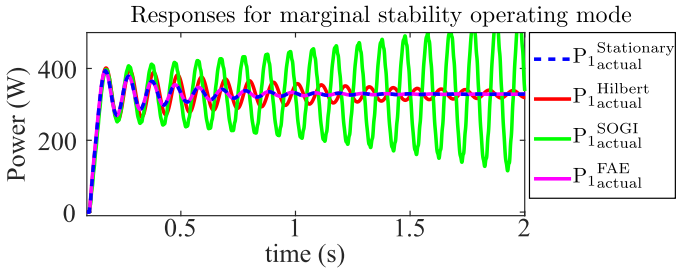

Fig. 16. Active power injections of the first inverter controlled in the stationary or rotating frame (*Scenario-II*).

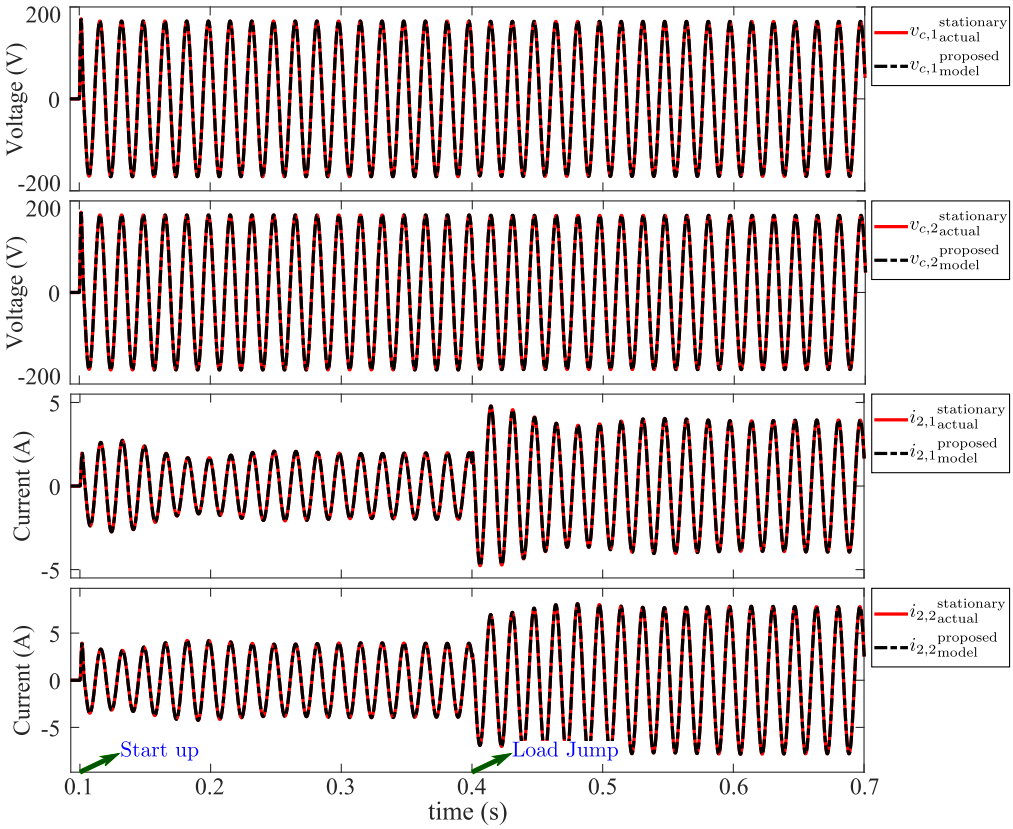

Fig. 17. Voltage and current waveforms of the actual system controlled in the stationary frame and the proposed large-signal (nonlinear) model predictions.

A. Stability Analysis of Microgrid

The linearized equations, presented in Appendix, are used for the small-signal stability analysis of a microgrid consisting of two inverters with numerical parameters represented in Table I that feed an RL load ($R = 28\,\Omega$ and $\mathrm{L} = 5$ mH). In this case ($N = 2$), the original system and the proposed model are of order 25 and 43, respectively. Also, Table II points out the parameters of the voltage and current controllers. Using the proposed small-signal (linearized) model, closed-loop poles of the system are calculated. Fig. 9 shows the dominant closed-loop poles for all those whose absolute values of their real parts are under $1000\,\mathrm{s}^{-1}$. All closed-loop poles are on the left side of complex plane, which means that the system is stable. The accuracy of the proposed and existing modeling approaches and also the impact of parameter variations on the system stability are studied now.

B. Model Verification

Scenario-I: In this scenario, first, the large-signal models' accuracy is assessed at nominal parameters represented in Table I. Fig. 10 shows the difference of active power injection of the first inverter P_1 between the models and actual system responses $\mathrm{e}_{\mathrm{P}_1} = \mathrm{P}_{1\mathrm{model}} - \mathrm{P}_{1\mathrm{actual}}$, for four cases: the system controlled in the stationary frame and its proposed model, and systems controlled in the rotating frame using the Hilbert transform, SOGI, and FAE for OSG and their models. The transfer functions of the

TABLE IV
PARAMETERS OF THE CCM INVERTER

	Inverter 3	
	Parameter	Value
	P_3^{nom}	500 W
	$L_{1,3}$	2.8 mH
	$C_{f,3}$	1.5 μF
	$L_{2,3}$	2 mH
Current Controller	$k_{c11,3}$	9×10^4
	$k_{c12,3}$	-4.28×10^4
	$k_{p11,3}$	22.6
	$k_{p12,3}$	0.14
	$k_{p13,3}$	-0.9

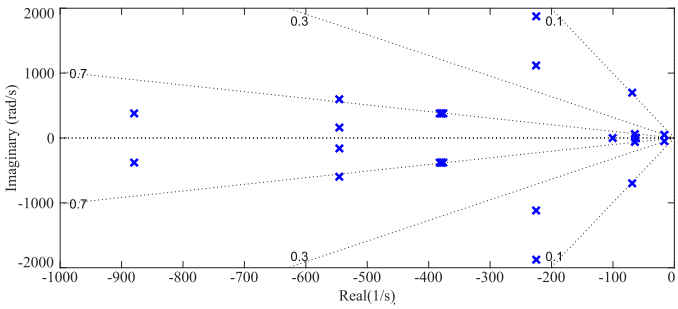

Fig. 18. Dominant poles of the system containing droop-controlled and CCM inverters obtained from the proposed small-signal (linearized) model.

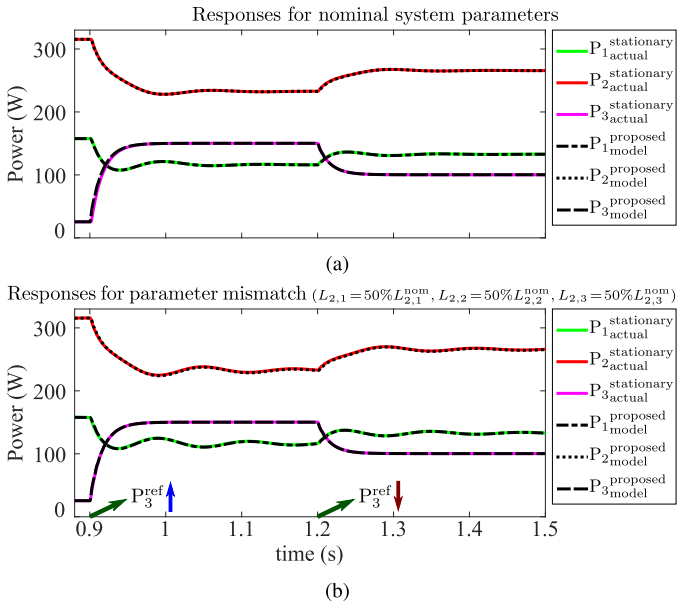

Fig. 19. Interactions among the CCM and droop-controlled inverters due to P_3^{ref} jumps and the proposed large-signal (nonlinear) model predictions (*Scenario-III*).

TABLE V
OSCILLATION FREQUENCY AND SYSTEM TIME CONSTANT IN MARGINAL STABILITY OPERATING MODE

	f_{osc}	τ
Proposed Small-signal Model	9.83 Hz	0.31 s
Simulation Results of Actual System	9.8 Hz	0.3 s
Experimental Results of Actual System	10.09 Hz	0.29 s

conventional OSG technique are also represented in Table III. As illustrated in Fig. 10(a)–(d), at nominal system parameters, all models predict the responses of their actual systems successfully, and error signals, shown in green for nominal system parameters, are damped to zero quickly.

Moreover, Fig. 10 compares the dynamic performance of the systems controlled in the stationary or rotating frames and their large-signal models accuracy when there is 30% mismatch between the nominal values and actual values of the load-side inductance of inverters, i.e., $L_{2,1}=70\%L_{2,1}^{\text{nom}}$ and $L_{2,2}=70\%L_{2,2}^{\text{nom}}$. According to this figure, the proposed model successfully represents the system controlled in the stationary frame in the presence of the inductance value mismatches. However, the system controlled in the rotating frame with FAE is much more sensitive to the parameter mismatches and becomes unstable. The reason is that the FAE is a model-based approach, which makes the FAE sensitive to system uncertainties. In fact, the mismatches between the nominal and actual system parameters lead to steady-state errors in the OSGs, which make the system responses more oscillatory than other OSG methods, such as the Hilbert transform and SOGI. That is why double-frequency oscillations appear on the active power injection characteristics, as shown in Fig. 10(d). However, this situation does not happen for the proposed approach because the imaginary system, used for deriving the accurate mathematical model, is not even implemented in the actual controller. Thus, it does not create sensitivity to uncertainties.

In addition, Fig. 11 compares active power responses of the first inverter, controlled either in the stationary or rotating frame, at the nominal parameters and when $L_{2,1}=70\%L_{2,1}^{\text{nom}}$ and $L_{2,2}=70\%L_{2,2}^{\text{nom}}$. Although the time responses of the systems are almost similar at the nominal parameters, as shown in Fig. 11(a), the system controlled in the rotating frame with FAE becomes unstable, as shown in Fig. 11(b), due to the model-based nature of the FAE method.

The impact of a parameter mismatch on the stability and performance of the aforementioned systems, controlled in either the stationary frame or the rotating frame, is studied in the following. For this purpose, it is assumed that the values of $L_{2,1}$ and $L_{2,2}$ vary from 100% to 40% of their nominal values $L_{2,1}^{\text{nom}}$ and $L_{2,2}^{\text{nom}}$ due to the system uncertainties, such as weak microgrid situations, saturation of the inductor cores, and so on. Fig. 12 shows how the dominant poles are affected due to the inductance value mismatches, which is obtained using the proposed small-signal (linearized) model. As depicted in this figure, the dominant poles move toward the marginal stability border. Also, the integral of absolute error (IAE) index [24] is used to compare the accuracy of the proposed large-signal (nonlinear) model for the system controlled in the stationary frame with large-signal (nonlinear) models for systems controlled in the rotating frame. For this purpose, IAE index is calculated for $e_{P_1}^{\text{proposed}}$, $e_{P_1}^{\text{Hilbert}}$, $e_{P_1}^{\text{SOGI}}$, and $e_{P_1}^{\text{FAE}}$ for different inductance value mismatches in a specific time period, as shown in Fig. 13. The proposed modeling approach has the minimum IAE index among the other existing modeling approaches, which indicates that the proposed model for single-phase systems controlled in the stationary frame is more reliable than models for systems controlled in the rotating frame for the stability analysis and studying the system behavior in the presence of parameter mismatches.

Scenario-II: In this scenario, the aforementioned systems are pushed close to the border of instability to the accuracy of the modeling approaches in this operating mode and to highlight how the undesirable dynamics of OSG methods affects the stability of the systems controlled in the rotating frame. For this purpose, the droop slope of the second inverter $m_{p,2}$ is increased to 0.015. Fig. 14 shows how the dominant poles change and approach to the instability border. The dominant poles are finally located at $\lambda = -3.197 \pm j61.77$. Fig. 15 shows the active power injection of the first and second inverters in the marginal stability operating mode when the actual system is controlled in the stationary frame and modeled using the proposed approach, and also for cases that the system is controlled in the rotating frame using the Hilbert transform, SOGI, or FAE for OSG and modeled in the rotating frame. The real part of the dominant poles predicts the response time constant of $\tau = \frac{1}{3.197} = 0.31$ s, which is confirmed in Fig. 15(a) ($\tau = 0.3$ s). Moreover, the imaginary part of the dominant poles indicates an oscillation at a frequency of 9.83 Hz, which matches the actual system response modeled by the proposed approach shown in Fig. 15(a), where $f_{\text{osc}} = 9.8$ Hz.

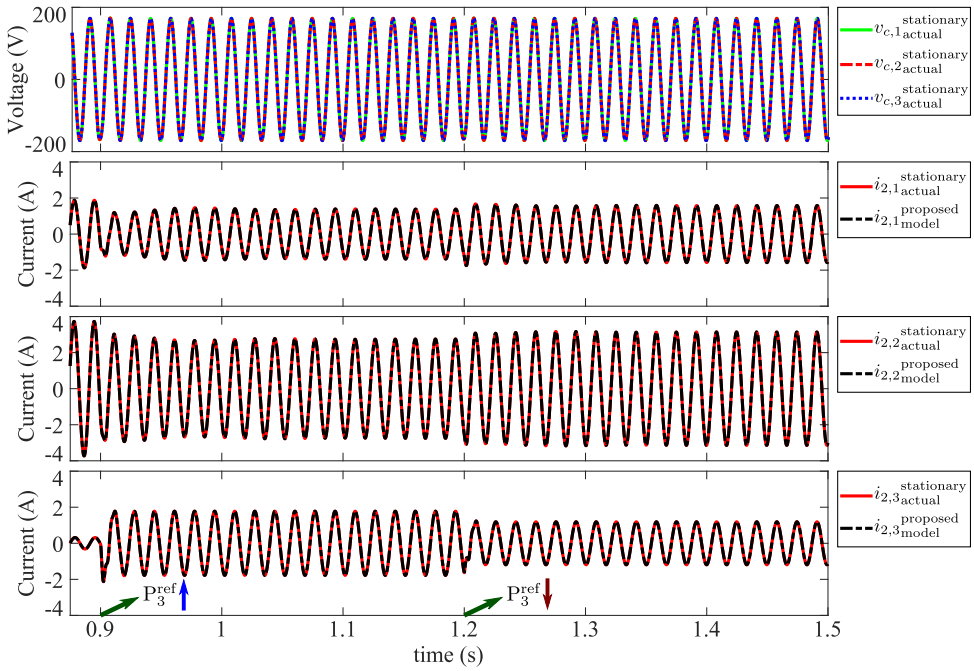

Fig. 20. Synchronous operations of CCM and droop-controlled inverters and the proposed large-signal (nonlinear) model predictions.

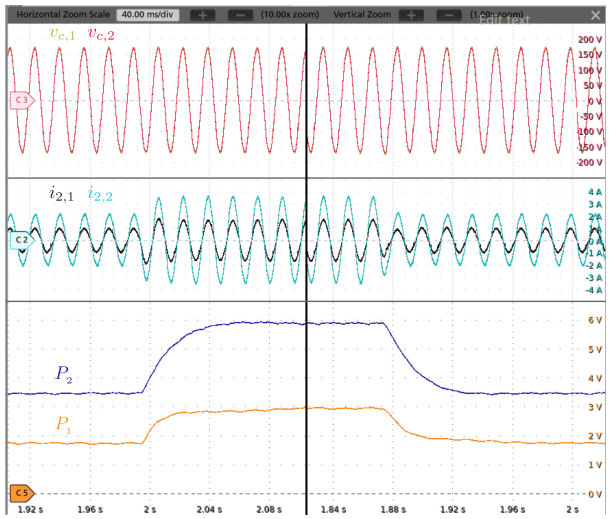

Fig. 21. Experimental results for the normal operating of two parallel inverters: load jumps and returns from 260 W and 40 VAr to 440 W and 80 VAr.

Furthermore, Fig. 16 shows active power injections of the first inverter, controlled either in the stationary or rotating frame, in the marginal stability operating mode. According to Figs. 15 and 16, the systems controlled in the rotating frame, which use the Hilbert transform or SOGI, become more oscillatory or unstable, and their responses do not match their large-signal model predictions. This is due to the undesirable OSG dynamics, which is overlooked in the design and stability analysis of the systems controlled in the rotating frame.

Scenario-III: In this scenario, the capability of the proposed modeling approach for predicting the internal-loops dynamics, i.e., voltage and current loops, is assessed. Fig. 17 shows current and voltage waveforms of the actual system controlled in the stationary frame and the proposed large-signal (nonlinear) model predictions. According to this figure, the parallel inverters start operating at $t=0.1$ s. Also, the system load varies from 500 W and 33 VAr to 985 W and 65 VAr at $t=0.4$ s. As shown in this figure, the proposed model can precisely represent the fast dynamic responses of the actual system controlled in the stationary frame as well. Moreover, the figure demonstrates that the parallel inverters are synchronized with each other.

To summarize, considering *Scenario-I* and *Scenario-II*, the system controlled in the stationary frame has wider stability margins than the system controlled in the rotating frame due to the undesired dynamics of OSG blocks, and the proposed modeling approach provides an accurate tool to analyze the stability of such system controlled in the stationary frame. Moreover, according to *Scenario-III*, the proposed approach is able to accurately predict and model the internal-loops dynamics.

VII. Interactions Among GFM and GFL Inverters

In the previous section, the interactions among droop-controlled inverters, GFM inverters, are studied, and the accuracy of the proposed modeling approach within different scenarios is verified. In the following, to cover a more general case, it is assumed that the microgrid, shown in Fig. 1, contains two droop-controlled inverters in addition to a current-controlled mode (CCM) inverter, GFL inverter.

In this case, the current control-loop equations of the CCM inverter can be derived in the stationary and rotating frames using the proposed approach as explained in Sections IV and V. The equation derivation process for the CCM inverter is not

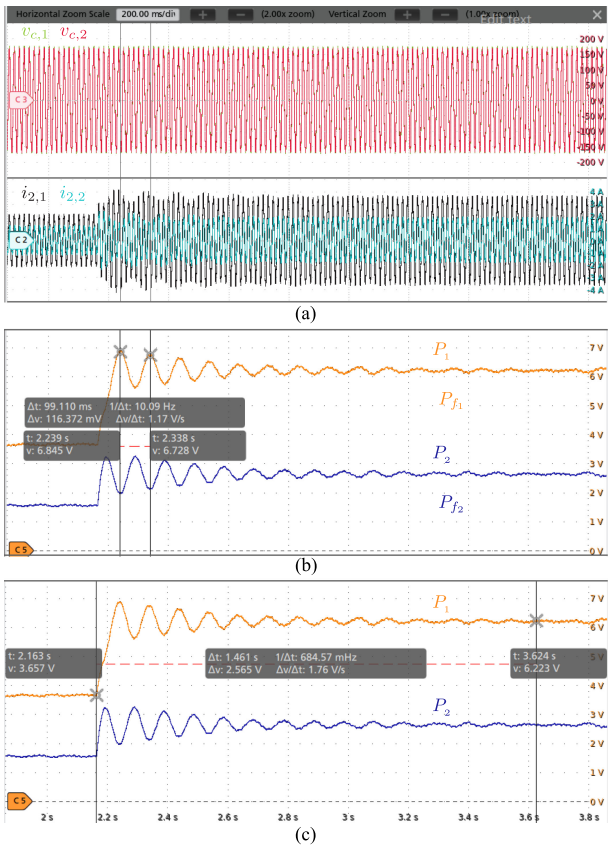

Fig. 22. Experimental results for the marginal stability operating mode with a droop coefficient of $m_{p,2} = 0.015$. (a) Current and voltage waveforms. (b) Oscillation frequency f_{osc}. (c) Time constant τ measurements.

repeated here to maintain the article's conciseness. Then, the equations of the CCM inverter are combined with the equations of droop-controlled inverters to form the microgrid equations in the stationary and rotating frames.

Similar to Section VI, the system equations in the rotating frame should be linearized for the small-signal stability analysis of the microgrid, which consists of two droop-controlled inverters and the CCM inverter whose parameters are listed in Table IV. In this case, the order of the original system equals 30, and the proposed model is of order 53. Fig. 18 shows the dominant closed-loop poles of the linearized system. As depicted in this figure, all poles fall in the left-hand complex plane, which indicates that the system is stable.

Fig. 19(a) shows a sample of the simulation results of the system operating at the nominal parameters and the proposed large-signal (nonlinear) model predictions. As shown in this figure, the reference power of the CCM inverter P_3^{ref} jumps from 25 to 150 W at $t = 0.6$ s. Then, P_3^{ref} decreases to 100 W at $t = 0.9$ s. It is observed that the proposed model accurately predicts system responses and the interactions among the different inverters. Moreover, Fig. 20 shows the synchronous operations of the CCM and droop-controlled inverters and also accurate predictions of the proposed model for the fast dynamics system responses.

Next, it is assumed that there is 50% mismatch among the nominal and actual values of the load-side inductances, i.e., $L_{2,1} = 50\% L_{2,1}^{\text{nom}}$, $L_{2,2} = 50\% L_{2,2}^{\text{nom}}$, and $L_{2,3} = 50\% L_{2,3}^{\text{nom}}$. Time responses of the system are shown in Fig. 19(b) for the same variations of P_3^{ref}. According to this figure, the proposed large-signal (nonlinear) model successfully represents the system controlled in the stationary frame in the presence of the inductance value mismatches as well.

To sum up, it is shown that not only can the proposed modeling approach be used to analyze the stability and to predict the time responses of the systems controlled in the stationary frame but also the proposed model is able to accurately predict the interactions among different types of inverters.

VIII. Experimental Results

In the experimental setup, the dc supplies are implemented with Chroma programmable dc power supply 62012P and Sorensen programmable power supply SGX500X10 C. The inverter controllers are implemented on dSPACE MicroLabBox (RTI 1202). For the numerical parameters in Table I, Fig. 21 illustrates the normal operating of two inverters with nested control loops (droop, voltage, and current control loops) when the system load jumps from 260 W and 40 VAr to 440 W and 80 VAr, and then, goes back to the previous condition.

In the next scenario, the system is pushed to the instability border by changing the droop slope of the second inverter $m_{p,2}$. Fig. 22 shows current and voltage waveforms, and active power injection of two inverters in the marginal stability operating mode. The oscillation frequency f_{osc} equals 10.09 Hz, and the system time constant τ equals $\frac{1.46}{5} = 0.29$ s. Comparing the experimental results, shown in Fig. 22, with the simulation results, shown in Fig. 14, confirms the accuracy of the proposed modeling approach. The oscillation frequency and time constant, obtained by the proposed small-signal (linearized) model, simulation, and experimental results, are listed in Table V.

IX. Conclusion

A method was proposed for modeling and stability analysis of a single-phase microgrid, including parallel inverters controlled in the stationary frame. The modeling was based on the introduction of an imaginary system to be augmented with the original system and form an equivalent system in the stationary frame based on α-axis and β-axis components. Therefore, using the method, all ac state variables can be converted to dc variables. The proposed modeling approach did not alter the eigenvalues, nor did it introduce time-varying terms. The accuracy of the proposed model was verified using simulation and experimental results. It was also shown that a single-phase system controlled in the stationary frame is more stable and robust than the same system controlled in the rotating frame due to drawbacks of inevitable OSG blocks in control loops.

Appendix

In this section, the small-signal (linearized) equations of the microgrid are derived with respect to the equations provided in

Section V to study the microgrid stability using the Jacobian matrix. Suppose $\mathbf{z}=[z_1 \ \cdots \ z_{l_z}]^T$, and $\mathbf{h}=[h_1 \ \cdots \ h_{l_h}]^T$ is a function on $\mathbf{z}$, where $\mathbf{h}: \mathbb{R}^{l_z} \rightarrow \mathbb{R}^{l_h}$. Thus, the Jacobian matrix of the function $\mathbf{h}$ is

$$\mathbf{J_h(z)} = \begin{bmatrix} \frac{\partial h_1(\mathbf{z})}{\partial z_1} & \cdots & \frac{\partial h_1(\mathbf{z})}{\partial z_{l_z}} \\ \vdots & \ddots & \vdots \\ \frac{\partial h_{l_h}(\mathbf{z})}{\partial z_1} & \cdots & \frac{\partial h_{l_h}(\mathbf{z})}{\partial z_{l_z}} \end{bmatrix}. \tag{A.1}$$

Now, consider $\mathbf{x}=[x_1 \ \cdots \ x_{l_1}]^T$, $\mathbf{u}=[u_1 \ \cdots \ u_{l_2}]^T$, and $\mathbf{y}=[y_1 \ \cdots \ y_{l_3}]^T$ as the state, input, and output vectors of a system, respectively, where $\dot{\mathbf{x}} = \mathbf{f}(\mathbf{x}, \mathbf{u})$ and $\mathbf{y} = \mathbf{g}(\mathbf{x}, \mathbf{u})$. In this case, using the Jacobian matrix (A.1), the linearized small-signal equations of the system are

$$\begin{aligned} &\dot{\widetilde{\mathbf{x}}} = \mathbf{A}^{(\mathrm{op})}\widetilde{\mathbf{x}} + \mathbf{B}^{(\mathrm{op})}\widetilde{\mathbf{u}}, \ \widetilde{\mathbf{y}} = \mathbf{C}^{(\mathrm{op})}\widetilde{\mathbf{x}} + \mathbf{D}^{(\mathrm{op})}\widetilde{\mathbf{u}} \\ &\mathbf{A}^{(\mathrm{op})} = \mathbf{J_f(x)}\Big|_{\substack{\mathbf{x}=\mathbf{X}^{(\mathrm{op})} \\ \mathbf{u}=\mathbf{U}^{(\mathrm{op})}}}, \mathbf{B}^{(\mathrm{op})} = \mathbf{J_f(u)}\Big|_{\substack{\mathbf{x}=\mathbf{X}^{(\mathrm{op})} \\ \mathbf{u}=\mathbf{U}^{(\mathrm{op})}}} \\ &\mathbf{C}^{(\mathrm{op})} = \mathbf{J_g(x)}\Big|_{\substack{\mathbf{x}=\mathbf{X}^{(\mathrm{op})} \\ \mathbf{u}=\mathbf{U}^{(\mathrm{op})}}}, \mathbf{D}^{(\mathrm{op})} = \mathbf{J_g(u)}\Big|_{\substack{\mathbf{x}=\mathbf{X}^{(\mathrm{op})} \\ \mathbf{u}=\mathbf{U}^{(\mathrm{op})}}}. \end{aligned} \tag{A.2}$$

The superscript "(op)" refers to the operating point, and the accent "$\sim$" denotes small-signal perturbations around the operating point. Eventually, the operating point can be obtained by numerically solving $\mathbf{f}(\mathbf{X}^{(\mathrm{op})}, \mathbf{U}^{(\mathrm{op})})=\mathbf{0}$ and $\mathbf{Y}^{(\mathrm{op})}=\mathbf{g}(\mathbf{X}^{(\mathrm{op})}, \mathbf{U}^{(\mathrm{op})})$.

According to the microgrid large-signal (nonlinear) model in the rotating frame shown in Fig. 8, (25)–(30), except (27), are explicitly nonlinear. Moreover, as ω_n is an output of the droop block, (22)–(24), and (31) are nonlinear as well due to the multiplication of ω_n to other system state variables or inputs. Therefore, (22)–(31) should be linearized around an operating point for the small-signal stability analysis by using (A.2).

The equations of the voltage and current loops (22) are linearized as

$$\begin{aligned} &\dot{\widetilde{\mathbf{x}}}_{vc,n}^{dq} = \mathbf{A}_{vc,n}^{dq(\mathrm{op})}\widetilde{\mathbf{x}}_{vc,n}^{dq} + \mathbf{B}_{vc,n}^{dq}\widetilde{v}_{c,n}^{\mathrm{ref}dq} + \mathbf{B}_{vL,n}^{dq}\widetilde{v}_L^{dq} + \cdots \\ &\qquad \cdots \mathbf{B}_{vc1,n}^{\omega_1(\mathrm{op})}\widetilde{\omega}_1 + \mathbf{B}_{vc2,n}^{\omega_n(\mathrm{op})}\widetilde{\omega}_n, \ \widetilde{\mathbf{y}}_{vc,n}^{dq} = \mathbf{C}_{vc,n}^{dq}\widetilde{\mathbf{x}}_{vc,n}^{dq} \\ &\mathbf{A}_{vc,n}^{dq(\mathrm{op})} = \mathbf{A}_{vc,n}^{dq}\Big|_{\omega_n=\omega_n^{(\mathrm{op})}}, \mathbf{B}_{vc1,n}^{\omega_1(\mathrm{op})} = \frac{\partial \mathbf{A}_{vc,n}^{dq}}{\partial \omega_1}\Big|_{\omega_n=\omega_n^{(\mathrm{op})}}\mathbf{X}_{vc,n}^{dq(\mathrm{op})} \\ &\mathbf{B}_{vc2,n}^{\omega_n(\mathrm{op})} = \begin{cases} \mathbf{0}, & n=1 \\ \frac{\partial \mathbf{A}_{vc,n}^{dq}}{\partial \omega_n}\Big|_{\omega_n=\omega_n^{(\mathrm{op})}}\mathbf{X}_{vc,n}^{dq(\mathrm{op})}, & n\neq 1. \end{cases} \end{aligned} \tag{A.3}$$

Regarding the APF block, its state-space equations (23) are linearized as

$$\begin{aligned} &\dot{\widetilde{\mathbf{x}}}_{ap,n}^{dq} = \mathbf{A}_{ap,n}^{dq(\mathrm{op})}\widetilde{\mathbf{x}}_{ap,n}^{dq} + \mathbf{B}_{ap,n}^{dq(\mathrm{op})}\widetilde{\mathbf{u}}_{ap,n}^{dq} + \mathbf{B}_{ap1,n}^{\omega_1(\mathrm{op})}\widetilde{\omega}_1 + \mathbf{B}_{ap2,n}^{\omega_n(\mathrm{op})}\widetilde{\omega}_n \\ &\widetilde{\mathbf{y}}_{ap,n}^{dq} = \mathbf{C}_{ap,n}^{dq}\widetilde{\mathbf{x}}_{ap,n}^{dq} + \mathbf{D}_{ap,n}^{dq}\widetilde{\mathbf{u}}_{ap,n}^{dq} \\ &\mathbf{A}_{ap,n}^{dq(\mathrm{op})} = \mathbf{A}_{ap,n}^{dq}\Big|_{\omega_n=\omega_n^{(\mathrm{op})}}, \mathbf{B}_{ap,n}^{dq(\mathrm{op})} = \mathbf{B}_{ap,n}^{dq}\Big|_{\omega_n=\omega_n^{(\mathrm{op})}} \\ &\mathbf{B}_{ap1,n}^{\omega_1(\mathrm{op})} = \frac{\partial \mathbf{A}_{ap,n}^{dq}}{\partial \omega_1}\Big|_{\omega_n=\omega_n^{(\mathrm{op})}}\mathbf{X}_{ap,n}^{dq(\mathrm{op})} \\ &\mathbf{B}_{ap2,n}^{\omega_n(\mathrm{op})} = \begin{cases} \frac{\partial \mathbf{B}_{ap,1}^{dq}}{\partial \omega_1}\Big|_{\omega_1=\omega_1^{(\mathrm{op})}}\mathbf{U}_{ap,1}^{dq(\mathrm{op})}, & n=1 \\ \frac{\partial \mathbf{A}_{ap,n}^{dq}}{\partial \omega_n}\Big|_{\omega_n=\omega_n^{(\mathrm{op})}}\mathbf{X}_{ap,n}^{dq(\mathrm{op})} + \frac{\partial \mathbf{B}_{ap,n}^{dq}}{\partial \omega_n}\Big|_{\omega_n=\omega_n^{(\mathrm{op})}}\mathbf{U}_{ap,n}^{dq(\mathrm{op})}, & n\neq 1. \end{cases} \end{aligned} \tag{A.4}$$

The equation of the virtual impedance block (24) is linearized as

$$\begin{aligned} &\widetilde{\mathbf{y}}_{\mathrm{vir},n}^{dq} = \mathbf{D}_{\mathrm{vir},n}^{dq(\mathrm{op})}\widetilde{\mathbf{u}}_{\mathrm{vir},n}^{dq} + \mathbf{D}_{\mathrm{vir},n}^{\omega_n(\mathrm{op})}\widetilde{\omega}_n, \mathbf{D}_{\mathrm{vir},n}^{dq(\mathrm{op})} = \mathbf{D}_{\mathrm{vir},n}^{dq}\Big|_{\omega_n=\omega_n^{(\mathrm{op})}} \\ &\mathbf{D}_{\mathrm{vir},n}^{\omega_n(\mathrm{op})} = \frac{\partial \mathbf{D}_{\mathrm{vir},n}^{dq}}{\partial \omega_n}\Big|_{\omega_n=\omega_n^{(\mathrm{op})}}\mathbf{U}_{\mathrm{vir},n}^{dq(\mathrm{op})}. \end{aligned} \tag{A.5}$$

For the power calculation block (25), the linearized equations are as

$$\begin{aligned} &\tilde{\mathbf{y}}_{pq,n} = \mathbf{D}_{pq,n}^{(\mathrm{op})}\tilde{\mathbf{u}}_{pq,n}^{dq}, \mathbf{D}_{pq,n}^{(\mathrm{op})} = \mathbf{J}_{\mathbf{g}_{pq,n}}(\mathbf{u}_{pq,n}^{dq})\big|_{\mathbf{u}_{pq,n}^{dq}=\mathbf{U}_{pq,n}^{dq(\mathrm{op})}} \\ &\mathbf{D}_{pq,n}^{(\mathrm{op})} = \begin{bmatrix} \frac{\partial g_{p,n}}{\partial i_{2,n}^d} & \frac{\partial g_{p,n}}{\partial i_{2,n}^q} & \cdots & \frac{\partial g_{p,n}}{\partial v_{cb,n}^d} & \frac{\partial g_{p,n}}{\partial v_{cb,n}^q} \\ \frac{\partial g_{q,n}}{\partial i_{2,n}^d} & \frac{\partial g_{q,n}}{\partial i_{2,n}^q} & \cdots & \frac{\partial g_{q,n}}{\partial v_{cb,n}^d} & \frac{\partial g_{q,n}}{\partial v_{cb,n}^q} \end{bmatrix}\Bigg|_{\mathbf{u}_{pq,n}^{dq}=\mathbf{U}_{pq,n}^{dq(\mathrm{op})}}. \end{aligned} \tag{A.6}$$

As the equations of the LPF block (27) are linear, the small-signal and large-signal equations are the same. Thus, the small-signal equations of the LPF are

$$\dot{\widetilde{\mathbf{x}}}_{lp,n} = \mathbf{A}_{lp,n}\widetilde{\mathbf{x}}_{lp,n} + \mathbf{B}_{lp,n}\widetilde{\mathbf{u}}_{lp,n}, \ \widetilde{\mathbf{y}}_{lp,n} = \mathbf{C}_{lp,n}\widetilde{\mathbf{x}}_{lp,n}. \tag{A.7}$$

As for the droop block equations, (30) is linearized as

$$\begin{aligned} &\dot{\widetilde{z}}_{d,n} = \mathbf{B}_{d,n}^{dq}\widetilde{\mathbf{u}}_{d,n}^{dq}, \ \widetilde{\mathbf{y}}_{d,n}^{dq} = \mathbf{C}_{d,n}^{dq(\mathrm{op})}\widetilde{z}_{d,n} + \mathbf{D}_{d,n}^{dq(\mathrm{op})}\widetilde{\mathbf{u}}_{d,n}^{dq} \\ &\mathbf{C}_{d,n}^{dq(\mathrm{op})} = \mathbf{J}_{\mathbf{g}_{d,n}}(z_{d,n})\Big|_{\substack{z_{d,n}=Z_{d,n}^{(\mathrm{op})} \\ \mathbf{u}_{d,n}^{dq}=\mathbf{U}_{d,n}^{dq(\mathrm{op})}}} \\ &\mathbf{D}_{d,n}^{dq(\mathrm{op})} = \begin{bmatrix} \mathbf{J}_{\mathbf{g}_{d,n}}(\mathbf{u}_{d,n}^{dq})\Big|_{\substack{z_{d,n}=Z_{d,n}^{(\mathrm{op})} \\ \mathbf{u}_{d,n}^{dq}=\mathbf{U}_{d,n}^{dq(\mathrm{op})}}} & \mathbf{D}_{3\,d,n}^{dq} \end{bmatrix}^T. \end{aligned} \tag{A.8}$$

Considering the droop-block equations, (29) and (30), as ω_n^{nl} and V_n^{nl} are constant values, their small-signal perturbations are equal to zero, i.e., $\widetilde{\omega}_n^{nl}=\widetilde{V}_n^{nl}=0$. In this case, the small-signal input vector of the droop block $\widetilde{\mathbf{u}}_{d,n}^{dq}$ is reduced to $\widetilde{\mathbf{u}}_{r_{d,n}}^{dq}=[\widetilde{P}_n \ \widetilde{Q}_n \ \widetilde{\omega}_1]^T$. Therefore, the linearized small-signal droop equations (A.8) are simplified as

$$\begin{aligned} &\dot{\widetilde{z}}_{d,n} = \mathbf{B}_{r_{d,n}}^{dq}\widetilde{\mathbf{u}}_{r_{d,n}}^{dq}, \ \widetilde{\mathbf{y}}_{d,n}^{dq} = \mathbf{C}_{d,n}^{dq(\mathrm{op})}\widetilde{z}_{d,n} + \mathbf{D}_{r_{d,n}}^{dq(\mathrm{op})}\widetilde{\mathbf{u}}_{r_{d,n}}^{dq} \\ &\mathbf{B}_{r_{d,n}}^{dq} = \begin{bmatrix} -m_{p,n} & 0 & -1 \end{bmatrix} \\ &\mathbf{C}_{d,n}^{dq(\mathrm{op})} = \begin{bmatrix} -V_n^{(\mathrm{op})}\sin Z_{d,n}^{(\mathrm{op})} & V_n^{(\mathrm{op})}\cos Z_{d,n}^{(\mathrm{op})} & 0 \end{bmatrix}^T \\ &\mathbf{D}_{r_{d,n}}^{dq(\mathrm{op})} = \begin{bmatrix} 0 & -m_{q,n}\cos Z_{12_n}^{(\mathrm{op})} & 0 \\ 0 & -m_{q,n}\sin Z_{d,n}^{(\mathrm{op})} & 0 \\ -m_{p,n} & 0 & 0 \end{bmatrix} \end{aligned} \tag{A.9}$$

where $V_n^{(\mathrm{op})} = V_n^{nl} - m_{q,n}Q_n^{(\mathrm{op})}$. Also, $\mathbf{B}_{r_{d,n}}^{dq}$ and $\mathbf{D}_{r_{d,n}}^{dq}$ in (A.8) refer to the reduced forms of $\mathbf{B}_{d,n}^{dq}$ and $\mathbf{D}_{d,n}^{dq}$ in (A.8).

Finally, the microgrid load equations, (31), are linearized as

$$\begin{aligned} &\dot{\widetilde{\mathbf{x}}}_L^{dq} = \mathbf{A}_L^{dq(\mathrm{op})}\widetilde{\mathbf{x}}_L^{dq} + \mathbf{B}_L^{dq}\widetilde{\mathbf{u}}_L^{dq} + \mathbf{B}_L^{\omega_1(\mathrm{op})}\widetilde{\omega}_1 \\ &\widetilde{\mathbf{y}}_L^{dq} = \mathbf{C}_L^{dq}\widetilde{\mathbf{x}}_L^{dq} + \mathbf{D}_L^{dq}\widetilde{\mathbf{u}}_L^{dq} \\ &\mathbf{A}_L^{dq(\mathrm{op})} = \mathbf{A}_L^{dq}\Big|_{\omega_1=\omega_1^{(\mathrm{op})}}, \mathbf{B}_L^{\omega_1(\mathrm{op})} = \frac{\partial \mathbf{A}_L^{dq}}{\partial \omega_1}\Big|_{\omega_1=\omega_1^{(\mathrm{op})}}\mathbf{X}_L^{dq(\mathrm{op})}. \end{aligned} \tag{A.10}$$

REFERENCES

[1] J. M. Guerrero, J. C. Vasquez, J. Matas, L. G. De Vicuna, and M. Castilla, "Hierarchical control of droop-controlled AC and DC microgrids—A general approach toward standardization," *IEEE Trans. Ind. Electron.*, vol. 58, no. 1, pp. 158–172, Jan. 2011.

[2] R. H. Lasseter, Z. Chen, and D. Pattabiraman, "Grid-forming inverters: A critical asset for the power grid," *IEEE Trans. Emerg. Sel. Topics Power Electron.*, vol. 8, no. 2, pp. 925–935, Jun. 2020.

[3] S. Yazdani, M. Ferdowsi, M. Davari, and P. Shamsi, "Advanced current-limiting and power-sharing control in a PV-based grid-forming inverter under unbalanced grid conditions," *IEEE Trans. Emerg. Sel. Topics Power Electron.*, vol. 8, no. 2, pp. 1084–1096, Jun. 2020.

[4] W. Duesterhoeft, M. W. Schulz, and E. Clarke, "Determination of instantaneous currents and voltages by means of alpha, beta, and zero components," *Trans. Amer. Inst. Elect. Engineers*, vol. 70, no. 2, pp. 1248–1255, 1951.

[5] Y. Sozer and D. A. Torrey, "Modeling and control of utility interactive inverters," *IEEE Trans. Power Electron.*, vol. 24, no. 11, pp. 2475–2483, Nov. 2009.

[6] S. Dasgupta, S. K. Sahoo, and S. K. Panda, "Single-phase inverter control techniques for interfacing renewable energy sources with microgrid—Part-I: Parallel-connected inverter topology with active and reactive power flow control along with grid current shaping," *IEEE Trans. Power Electron.*, vol. 26, no. 3, pp. 717–731, Mar. 2011.

[7] R. I. Bojoi, L. R. Limongi, D. Roiu, and A. Tenconi, "Enhanced power quality control strategy for single-phase inverters in distributed generation systems," *IEEE Trans. Power Electron.*, vol. 26, no. 3, pp. 798–806, Mar. 2011.

[8] B. Bahrani, A. Rufer, S. Kenzelmann, and L. A. Lopes, "Vector control of single-phase voltage-source converters based on fictive-axis emulation," *IEEE Trans. Ind. Appl.*, vol. 47, no. 2, pp. 831–840, Mar./Apr. 2011.

[9] M. Ebrahimi, S. A. Khajehoddin, and M. Karimi-Ghartemani, "Fast and robust single-phase *DQ* current controller for smart inverter applications," *IEEE Trans. Power Electron.*, vol. 31, no. 5, pp. 3968–3976, May 2016.

[10] H. Abu-Rub, M. Malinowski, and K. Al-Haddad, *Power Electronics for Renewable Energy Systems, Transportation and Industrial Applications*. Hoboken, NJ, USA: Wiley, 2014.

[11] L. Xinchun, F. Feng, D. Shanxu, K. Yong, and C. Jian, "Modeling and stability analysis for two paralleled UPS with no control interconnection," in *Proc. IEEE Int. Elect. Mach. Drives Conf.*, 2003, pp. 1772–1776.

[12] J. Rocabert, A. Luna, F. Blaabjerg, and P. Rodriguez, "Control of power converters in AC microgrids," *IEEE Trans. Power Electron.*, vol. 27, no. 11, pp. 4734–4749, Nov. 2012.

[13] S. A. Khajehoddin, M. Karimi-Ghartemani, and M. Ebrahimi, "Grid-supporting inverters with improved dynamics," *IEEE Trans. Ind. Electron.*, vol. 66, no. 5, pp. 3655–3667, May 2019.

[14] M. N. Marwali, J.-W. Jung, and A. Keyhani, "Stability analysis of load sharing control for distributed generation systems," *IEEE Trans. Energy Convers.*, vol. 22, no. 3, pp. 737–745, Sep. 2007.

[15] X. Wang, L. Harnefors, and F. Blaabjerg, "Unified impedance model of grid-connected voltage-source converters," *IEEE Trans. Power Electron.*, vol. 33, no. 2, pp. 1775–1787, Feb. 2018.

[16] A. Yazdani and R. Iravani, *Voltage-Sourced Converters in Power Systems*. Hoboken, NJ, USA: Wiley Online Library, 2010, vol. 39.

[17] M. N. Marwali and A. Keyhani, "Control of distributed generation systems–Part I: Voltages and currents control," *IEEE Trans. Power Electron.*, vol. 19, no. 6, pp. 1541–1550, Nov. 2004.

[18] N. Pogaku, M. Prodanovic, and T. C. Green, "Modeling, analysis and testing of autonomous operation of an inverter-based microgrid," *IEEE Trans. Power Electron.*, vol. 22, no. 2, pp. 613–625, Mar. 2007.

[19] R. Rosso, X. Wang, M. Liserre, X. Lu, and S. Engelken, "Grid-forming converters: Control approaches, grid-synchronization, and future trends—A review," *IEEE Open J. Ind. Appl.*, vol. 2, pp. 93–109, 2021.

[20] S. A. Khajehoddin, M. Karimi-Ghartemani, and M. Ebrahimi, "Optimal and systematic design of current controller for grid-connected inverters," *IEEE Trans. Emerg. Sel. Topics Power Electron.*, vol. 6, no. 2, pp. 812–824, Jun. 2018.

[21] J. M. Guerrero, J. C. Vasquez, J. Matas, M. Castilla, and L. G. de Vicuna, "Control strategy for flexible microgrid based on parallel line-interactive UPS systems," *IEEE Trans. Ind. Electron.*, vol. 56, no. 3, pp. 726–736, Mar. 2009.

[22] J. M. Guerrero, L. G. De Vicuna, J. Matas, M. Castilla, and J. Miret, "Output impedance design of parallel-connected UPS inverters with wireless load-sharing control," *IEEE Trans. Ind. Electron.*, vol. 52, no. 4, pp. 1126–1135, Aug. 2005.

[23] O. V. Kulkarni, S. Doolla, and B. Fernandes, "Simple controller configuration for decentralized parallel operation of inverters," *IEEE Trans. Power Electron.*, vol. 34, no. 2, pp. 1356–1369, Feb. 2019.

[24] R. C. Dorf and R. H. Bishop, *Modern Control Systems*. Upper Saddle River, NJ, USA: Pearson, 2011.

Nima Amouzegar Ashtiani (Graduate Student Member, IEEE) received the B.Sc. degree in electrical power engineering from the Amirkabir University of Technology, Tehran, Iran, in 2012, and the M.Sc. degree in electrical power engineering from the Sharif University of Technology, Tehran, Iran, in 2014. He is currently working toward the Ph.D. degree with the University of Alberta, Edmonton, AB, Canada.

His research interests include control, modeling, stability analysis, and efficiency improvement of power converters and microgrids.

S. Ali Khajehoddin (Senior Member, IEEE,) received the B.Sc. and M.Sc. degrees in electrical engineering from the Isfahan University of Technology, Isfahan, Iran, in 1997 and 2000, respectively, and the Ph.D. degree in electrical engineering specialized in power electronics and their applications in renewable energy systems from Queen's University, Kingston, ON, Canada, in April 2010.

After completing the master's degree, he co-founded a startup company, which was focused on the development and production of power analyzers and smart metering products used for smart grid applications. For the Ph.D. research with Queen's University, he focused on the design and implementation of compact and durable microinverters for photovoltaic grid-connected systems. Based on this research, Queen's University spun off SPARQ systems, Inc., where, as the Lead Research and Development Engineer, he worked toward mass production and commercialization of microinverters from 2010 to 2013. He joined the Department of Electrical and Computer Engineering, University of Alberta, Edmonton, AB, Canada, in 2013.

Dr. Khajehoddin is currently an Associate Editor for the IEEE TRANSACTIONS ON POWER ELECTRONICS, IEEE TRANSACTIONS ON SUSTAINABLE ENERGY, and IEEE JOURNAL OF EMERGING AND SELECTED TOPICS IN POWER ELECTRONICS.

Masoud Karimi-Ghartemani (Senior Member, IEEE) received the Ph.D. degree in electrical engineering from the University of Toronto, Toronto, ON, Canada, in 2004.

From 2005 to 2008, he was a Faculty Member with the Department of Electrical Engineering, Sharif University of Technology, Tehran, Iran. From 2008 to 2011, he was a member of the ePOWER Laboratory, Queen's University, Kingston, ON, Canada. Since 2012, he has been with the Department of Electrical and Computer Engineering, Mississippi State University (MSU), Starkville, MS, USA, where he is currently a Professor. His research interests include modeling and control of distributed and renewable energy systems.

Dr. Karimi was a recipient of the 2020 Faculty Research Award at MSU's Bagley College of Engineering. He is currently an Associate Editor for the IEEE TRANSACTIONS ON INDUSTRIAL ELECTRONICS, IEEE TRANSACTIONS ON SUSTAINABLE ENERGY, and IEEE Power and Energy Letters.